Magnetic Mineral Diagenesis in a Newly Discovered Active Cold Seep Site in the Bay of Bengal

F. Badesab*, P. Dewangan and V. Gaikwad

Geological Oceanography Division, CSIR- National Institute of Oceanography, Dona Paula, Goa, India

Diagenetically formed magnetic minerals at marine methane seep sites are potential archive of past fluid flow and could provide important constraints on the evolution of past methane seepage dynamics and gas hydrate formation over geologic time. In this study, we carried out integrated rock magnetic, and mineralogical analyses, supported by electron microscope observations, on a seep impacted sediment core to unravel the linkage between greigite magnetism, methane seepage dynamics, and evolution of shallow gas hydrate system in the K-G basin. Three sediment magnetic zones (MZ-1, MZ-2, and MZ-3) have been identified based on the down-core variations in rock magnetic properties. Two events of intense methane seepage are identified. Repeated occurences of authigenic carbonates throughout the core indicate the episodic intensification of anaerobic oxidation of methane (AOM) at the studied site. Marked depletion in magnetic susceptibility manifested by the presence of chemosynthetic shells (*Calyptogena* Sp.), methane-derived authigenic carbonates, and abundant pyrite grains provide evidences on intense methane seepage events at this site. Fracture-controlled fluid transport supported the formation of gas hydrates (distributed and massive) at this site. Three greigite bearing sediment intervals (G1, G2, G3) within the magnetically depleted zone (MZ-2) are probably the paleo-gas hydrate (distributed-type vein filling) intervals. A strong linkage among clay content, formation of veined hydrate deposits, precipitation of authigenic carbonates and greigite preservation is evident. Hydrate crystallizes within faults/fractures formed as the methane gas migrates through the gas hydrate stability zone (GHSZ). Formation of authigenic carbonate layers coupled with clay deposits restricted the upward migrating methane, which led to the formation of distributed-type vein filling hydrate deposits. A closed system created by veined hydrates trapped the sulfide and limited its availability thereby, causing arrestation of pyritization and favored the formation and preservation of greigite in G1, G2, G3.

Keywords: cold, seep, methane hydrate, rock magnetism, diagenesis, Bay of Bengal

INTRODUCTION

Cold seep ecosystems are unique ecosystem characterized by ebullition of methane-rich fluids through the seafloor (Suess, 2014). At active seeps, sulfate reduction driven by anaerobic oxidation of methane (AOM) releases sufficient amount of hydrogen sulfide into the surrounding pore waters (Borowski et al., 1996; Jørgensen et al., 2004) to sustain chemosynthetic communities. The hydrogen sulfide also facilitate dissolution of primary detrital magnetic minerals and transform them into stable non-magnetic pyrite or intermediate ferrimagnetic greigite; thereby, generating secondary magnetic signals in the host sediments (Housen and Musgrave, 1996; Passier et al., 1998; Kasten et al., 2003; Neretin et al., 2004; Riedinger et al., 2005; Musgrave et al., 2006; Larrasoaña et al., 2007; Roberts et al., 2015). These magnetic minerals serve as an excellent geological archive to record past methane seepage, and help in understanding the geochemical processes that favor diagenesis of magnetic mineral and may also influence the gas hydrate dynamics (formation and dissociation) (Housen and Musgrave, 1996; Aharon et al., 1997; Musgrave et al., 2006; Larrasoaña et al., 2007; Bayon et al., 2013; Feng and Chen, 2015).

Active seeps are also associated with shallow gas hydrates deposits (Bohrmann et al., 1998; Greinert et al., 2001; Suess, 2014; Bayon et al., 2015). These deposits undergo several cycles of formation and dissociation to sustain themselves within the sediment column (Chuvilin et al., 2018). Destabilization of gas hydrates due to increase in pressure owing to sedimentation, burial and tectonic activities can release vast amount of methane; a fraction of which may rise up to seafloor and form cold seep (Haq, B.U, 1998; Henriet et al., 1998; Vogt and Jung, 2002; Sultan et al., 2004; Handwerger et al., 2017; Argentino et al., 2019). Diagenesis of magnetic minerals involves postdepositional changes either by altering the detrital magnetic mineral assemblages or through authigenic growth of secondary minerals (Roberts, 2015; Musgrave et al., 2019). Therefore, the sediment magnetic signals in marine sedimentary system represent the primary depositional and secondary diagenetic processes. In methane-rich sediments, hydrogen sulfide generated via AOM at the sulfate-methane transition zone (SMTZ) can cause dissolution of iron oxides and precipitation of iron sulfides including ferrimagnetic greigite, pyrrhotite and culminating toward formation of pyrite (Kasten et al., 1998; Jørgensen et al., 2004; Kao et al., 2004; Neretin et al., 2004). Greigite can survive the pyritization process in the regions containing limited sulfide concentration. For example in gas hydrate bearing sediments of Cascadia Margin and Nankai Trough, it was demonstrated that sulfide sometime gets trapped within hydrate itself causing further arrestation of pyritization processes and subsequent precipitation of greigite and pyrrhotite (Housen and Musgrave, 1996; Kars and Kodama, 2015). Therefore, ferrimagnetic iron sulfide minerals (greigite, pyrrhotite) formed during such processes are regarded as potential markers of fossil gas hydrate deposits, and identification of such magnetic minerals may also help in deciphering paleo-gas hydrate deposits in marine sediments (Larrasoaña et al., 2007).

The first evidence of active methane seepage and shallow methane hydrate from geological, geochemical and geophysical studies was reported by Mazumdar et al. (2019) in the Krishna-Godavari (K-G) basin. Gas hydrate exploration cruise (SSD-045) of CSIR-National Institute of Oceanography (CSIR-NIO) onboard R/V Sindhu Sadhana discovered this active seep and associated shallow gas hydrates in 2018 (**Figure 1A**). Fracture-filled gas hydrates were recovered from sediment depth interval of 305–315 cmbsf at this site (Stn-9), (**Figure 1B**). The seep occurs due to deformation structures (fault/fractures and diapirs) formed due to shale tectonism in K-G basin (Dewangan et al., 2010; Sriram et al., 2020). A high-resolution seismic data beneath the seep sites showed the presence of acoustic chimneys, and the overburden is heavily faulted (Dewangan et al., 2020). Deep-rooted faults provide a conducive environment for the migration of methane from deep-seated gas reservoir and led to the development of a cold seep ecosystem and formation of shallow fracture-filled gas hydrate deposits at the studied site (Dewangan et al., 2020; Mazumdar et al., 2019; Sriram et al., 2020). High methane flux and favourable P-T conditions supported the accumulation of gas hydrates (Mazumdar et al., 2019). A recent rock magnetic study by Badesab et al. (2019) on the long drilled sediment cores that overlie the deep-seated gas hydrate deposit provided the longest and most detailed sediment magnetic record in the K-G basin, Bay of Bengal. They successfully delineated the control of higher sedimentation events and shale tectonics on the development of fracture-filled gas hydrate deposit and magnetic mineral diagenesis in K-G basin. A magnetic based proxy to constrain paleo-methane seepage events in marine sediments was established. In the present study, we carried out integrated rock magnetic and mineralogical analyses along with electron microscope observations on the seep impacted sediment core (SSD-045/Stn-9/GC-01) to unravel the linkage between greigite magnetism, methane seepage dynamics, and evolution of shallow gas hydrate system in the K-G basin. This 3.16 m long sediment gravity core serves as a potential archive to constrain the methane seepage dynamics and to understand the processes governing the shallow gas hydrate formation/dissociation through recent geologic time.

GEOLOGICAL SETTING

The K-G basin is a pericratonic, petroliferous rift basin located in the eastern continental margin of India (Powell et al., 1988). The sediment thicknesses reported from K-G basin varies from 3 to 5 km in the onshore region to about 8 km in the offshore region (Prabhakar and Zutshi, 1993; Bastia, 2007). Majority of sediment load to the basin is delivered by the Krishna and Godavari rivers (Rao, 2001). Annual sediment transport of the Krishna and Godavari rivers is estimated to be around 67.7 and 170 × 106 t, respectively (Biksham and Subramanian, 1988; Ramesh and Subramanian, 1988). Sedimentary deposits in the K-G basin are dominated by smectite-bearing Godavari clay formations (Rao, 2001). Krishna and Godavari rivers and their tributaries originates in the Western Ghats and drains through the

FIGURE 1 | (A) Map showing the location of sediment core (SSD-045/Stn-0/GC-01) in the Krishna-Godavari (K-G) basin, Bay of Bengal and **(B)** photograph of recovered gas hydrate (GH) sample. Bathymetry data of the studied area was obtained from GEBCO Compilation Group (2020) GEBCO 2020 Grid (doi: 10.5285/a29c5465-b138-234d-e053-6c86abc040b9).
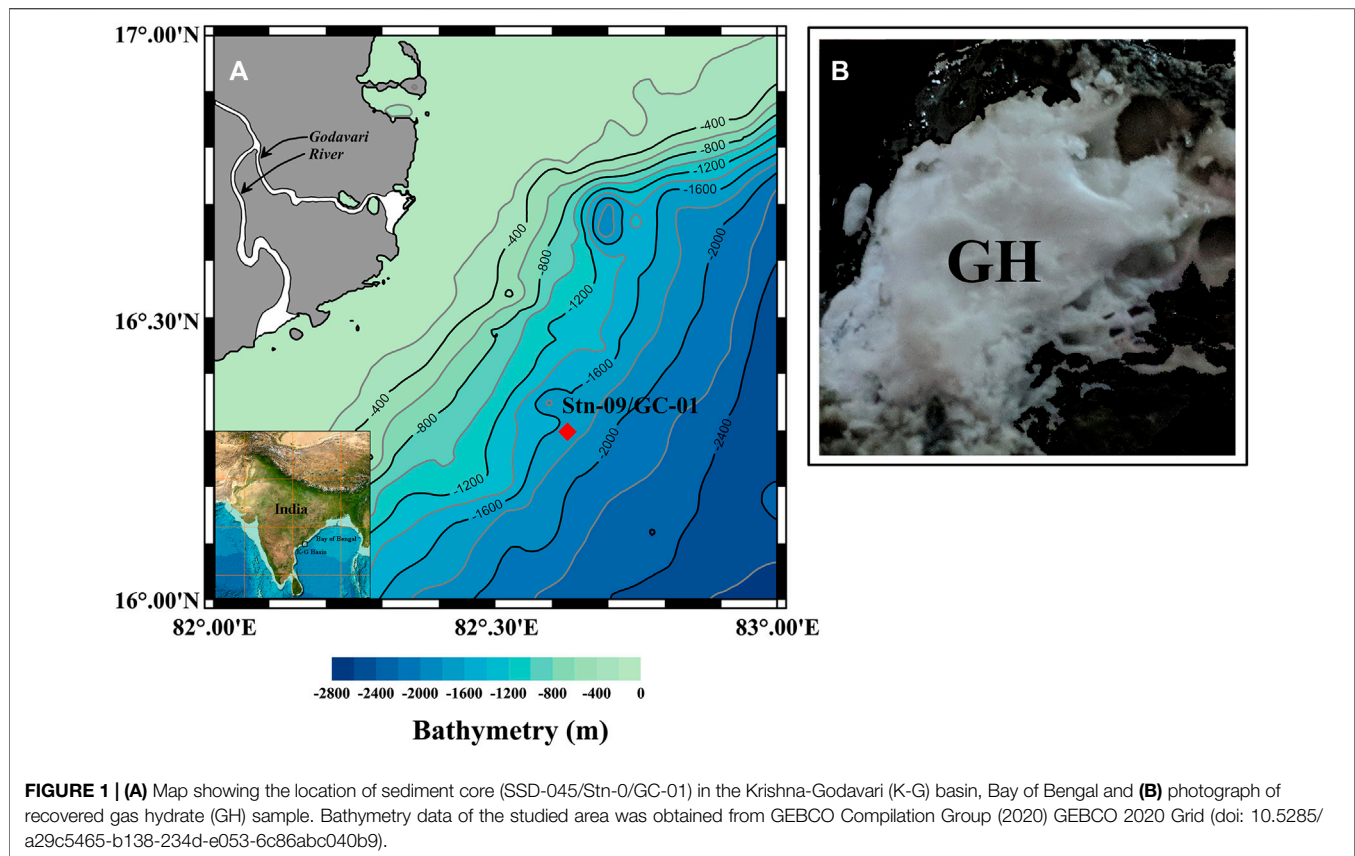
provenance of Deccan trap basalts and Precambrian metamorphic rocks and created a thick sediment strata containing the dominant montmorillonite clay with traces of illite and kaolinite (Rao, 1991). Krishna and Godavari rivers are the major supplier of magnetite-rich detrital load to the K-G basin and hence provide an excellent opportunity to conduct studies related to environmental magnetism (Ramesh and Subramanian 1988; Sangode et al., 2007).

The K-G basin shows deformation structures in the form of shale bulges and toe-thrust faults due to ongoing gravity-driven shale tectonism (Choudhuri et al., 2010; Dewangan et al., 2010). One of the reasons for shale tectonism is rapid sedimentation during Paleocene and Eocene, which led to overpressured shale strata in the K-G basin (Rao and Mani, 1993; Singha and Chatterjee, 2014). The detrital load in the deltaic regions led to the movement of deeply buried shale strata and several geomorphic structures like bathymetric mounds, sedimentary ridges and toe-thrust faults formed on the sea floor. These deformed structures provide efficient migration pathway for methane-rich fluids through the deep-rooted faults, and hence these regions are preferred locales for the formation of gas hydrates deposits (Dewangan et al., 2010). The presence of sub-surface gas hydrate deposits in the K-G basin has been confirmed through well-logging, drilling and sediment coring activities, while paleo-methane seepage events are evident through the presence of methane derived authigenic

carbonates and chemosynthetic community (Collett et al., 2008; Mazumdar et al., 2009, 2019).

MATERIALS AND METHODS

Coring Site, Sampling and Measurements

Gravity core (SSD-045/Stn-9/GC-01) was recovered onboard R/V Sindhu Sadhana (cruise no: SSD-045) from the K-G offshore basin (Latitude: 16°18.6027'N; Longitude: 82°37.9809'E; water depth: 1,673 m; core length: 3.16 m). The core was sub-sampled at the every 2 cm interval. Light gray to deep black colored soft sediments in this core yielded a strong odor of hydrogen sulfide after opening the sediment core onboard. The vertical sediment distribution in this core showed the dominance of clay and silt sized fractions. Numerous layers of light gray colored authigenic carbonates were found throughout the core. Dead shells of *Calyptogena* Sp. were found at 27 cmbsf and 51 cmbsf in the studied sediment core. Fracture-filled type gas hydrates were recovered from the core catcher and bottommost sediment interval at this site. Sediment sub-sampling for magnetic measurements were carried out in presence of high purity nitrogen flushing to avoid atmospheric conditions which could oxidize hydrogen sulfide or iron mono-sulfide present in the sediments. For rock magnetic analysis, 158 sub-wet sediment samples were weighed, and packed in a 25 mm cylindrical plastic sample bottles. Measurements were carried out

at the Paleomagnetic laboratory of CSIR-National Institute of Oceanography (NIO), Goa, India and Center for Advanced Marine Core Research (CMCR), Kochi University, Japan.

Rock Magnetic Analysis

Low-field low frequency (0.47 kHz) magnetic susceptibility (χ) was measured using a MS2B Bartington Instruments magnetic susceptibility meter. An anhysteretic remanent magnetization (ARM) was applied in a direct current bias field (50 μT) in the presence of 100 mT peak alternating field and the remanent magnetism was measured using an AGICO JR-6A automatic spinner magnetometer. An isothermal remanent magnetization (IRM) was applied in an inducing field of +1 T in the forward direction and was demagnetized by DC backfields at −20, −30, −100, and −300 mT using a MMPM10 pulse magnetizer. The respective remanences were measured using AGICO JR-6A automatic spinner magnetometer. Mass-normalized IRM acquired at a peak field of 1T is considered to be the saturation IRM (SIRM). S-ratio is calculated as the ratio between the IRM at −300 mT and SIRM (IRM$_{-300mT}$/SIRM$_{1T}$; Bloemendal et al., 1992). This ratio indicates the relative proportion of high coercivity minerals compared to soft ferrimagnetic minerals. Thermomagnetic measurements were carried out at Paleo and Rock Magnetism Laboratory of CMCR. About 12 selected dried sediment samples were analyzed on a Natsuhara Giken (Model NMB-89) magnetic balance (Range: Room temperature to 700°C) with a heating rate of 10°C/min in a 0.3-T field. Hysteresis loops, first-order reversal curves (FORC) and back-field demagnetization curves were also measured for 10 selected dried sediment samples with a saturating field of 1 T (averaging time of 200 ms, slew rate limit of 1 T/, and field increment of 4 mT) at the CMCR. FORC distributions were generally processed using a smoothing factor (SF) of 4, but SF = 6 was used where possible (Roberts et al., 2000). FORC diagrams (Pike et al., 1999) were processed using the FORCinel software (Harrison and Feinberg, 2008).

Low-temperature magnetic measurements were made on six selected dried sediment samples with a Quantum Design Magnetic Properties Measurement System at CMCR. A RT-SIRM was imparted at room temperature (300 K) in 2.5 T. Samples were later cooled to 5 K and warmed back to 300 K in a zero magnetic field. A LT-SIRM was then applied at 5 K in 2.5 T. Samples were warmed up to 300 K in a zero magnetic field (termed "ZFC" for zero field-cooled). Samples were then cooled to 5 K in the presence of a 2.5 T magnetic field. A LT-SIRM was again imparted at 5 K, and samples were warmed to 300 K in a zero magnetic field (termed "FC" for field-cooled). Magnetic parameters were normalized by sample mass. Derived parameters (δ_{FC} and δ_{ZFC}) were calculated following Moskowitz et al. (1993).

Sedimentological Analyses
Bulk Sediment Grain Size Measurements

Sediment grain size measurements were performed on a Laser Particle Size Analyzer (Malvern Mastersizer 2000) at CSIR-NIO. For removal of carbonate content, desalinated sediment samples were treated using dilute HCl (1N). Further, same suspensions

were treated with 10% H_2O_2 to remove organic carbon content. The sediment dispersing agent (Na-hexametaphosphate) was added to the suspension before the analyses. Grain size values are presented as volume %.

Mineralogical Investigations

Magnetic particles were extracted from the bulk sediment following Petersen et al. (1986). A scanning electron microscope (SEM; JEOL JSM-5800 LV) captured the images of magnetic particles in a secondary electron imaging mode at energy levels between 15 and 20 keV. An energy dispersive X-ray spectroscopy (EDS) probe attached to the microscope was used to determine the composition of magnetic particles. The magnetic mineralogy of the selected samples from different sediment magnetic zones was determined using a Rigaku X-Ray Diffractometer (Ultima IV). The samples were run from 15° to 70° of 2θ at 1°/min scan speed using Cu Kα radiation (λ = 1.5414 Å).

Authigenic Carbonates and Chemosynthetic Community

Authigenic carbonates and chemosynthetic shells (*Calyptogena* sp.) were hand-picked during sub-sampling of the sediment core. These materials were washed and cleaned using a distilled water, and later dried at room temperature and stored in the plastic container.

RESULTS

Down-Core Changes in Magnetic Profile

We broadly classified the rock magnetic profile of the sediment core SSD-045/Stn-9/GC-01 into three distinct sediment magnetic zones: MZ-1 (uppermost 23.0 cmbsf), MZ-2 (25.0–265.0 cmbsf), and MZ-3 (267.0–315.0 cmbsf) based on the down core changes in the magnetic mineral concentration, composition and granulometry data. χ_{lf}, ARM, and SIRM (**Figures 2A–C**) are generally used as a diagnostic for magnetic mineral concentration. In MZ-1, a systematic decrease in these parameters from 1 to 5 cmbsf indicate down-core reduction in the magnetic mineral concentration (**Figures 2A–C**). MZ-1 showed higher values of χ_{lf}, ARM and SIRM suggesting high concentration of magnetic minerals while lower values are observed in MZ-2 and show uniform values except at certain intervals (**Figures 2A–C**). The beginning of MZ-2 is marked by an abrupt decrease in the magnetite concentration, and we refer this interval as the zone of reduced magnetic susceptibility (χ_{lf}). Within this zone (MZ-2), three distinct sediment intervals (G1, G2, G3) showed minor rise in χ_{lf}, ARM, SIRM, and SIRM/χ_{lf} indicating the dominance of fine-grained (SP-size) ferrimagnetic particles (**Figures 2A–C,E**; Tarduno, 1995; Rowan et al., 2009).

The SIRM/χ_{lf} ratio, an indicator of grain size of magnetic iron sulfides (Peters and Thompson, 1998; Peters and Dekkers, 2003) showed a linear decrease in MZ-1 and MZ-2 with a noticeable rise in G1, G2, G3 intervals and the bottommost sediment interval (303.0–315.0 cmbsf) in MZ-3 indicating the presence of fine-grained magnetic particles (**Figure 2E**). The variations in S-ratio can be linked to the changes in magnetic mineralogy, and

FIGURE 2 | Depth variations of selected rock magnetic data **(A–F)** for sediment core (SSD-045/Stn-9/GC-01). Data from discrete parameters are color-coded as magnetic susceptibility χ_{lf} (red), anhysteretic remanent magnetization (ARM) (blue), saturation isothermal remanent magnetization (SIRM) (orange), ARM/SIRM (purple), SIRM/χ_{lf} (brown), and S-ratio (green). Based on the variation in magnetic susceptibility, three sedimentary magneto-zones MZ-1, MZ-2, and MZ-3 are demarcated. Greigite bearing sediment intervals (G1, G2, and G3) are highlighted with yellow shading. Gas hydrate bearing bottom-most interval in MZ-3 is highlighted by green shading. AGC refers to authigenic carbonates.

is generally high and close to unity throughout the core (**Figure 2F**). A noticeable drop in S-ratio is observed between 229 cmbsf to 241 cmbsf suggesting the presence of either higher coercivity magnetic mineral (hematite, goethite) or ferrimagnetic magnetic iron sulfides (greigite, pyrrhotite) in this interval (**Figure 2F**) (Peters and Dekkers, 2003; Roberts et al., 2011).

Thermomagnetic Analyses

Thermomagnetic experiments on the representative sediment samples from MZ-1, MZ-2, MZ-3, G1, G2, and G3 are shown in **Figure 3**. A major drop in magnetization between 563°C and 595°C except on G3 sample (**Figure 3I**) suggest that the magnetite is the dominant magnetic mineral present in the sediments (Özdemir and Dunlop, 1997; **Figures 3A–J**). Increase in χ between 332°C and 480 °C can be attributed to the conversion of paramagnetic minerals into magnetite during heating process (Hirt et al., 1993; Passier et al., 2001; Philips, 2018; **Figures 3A–J**).

First-Order Reversal Curves Diagrams

FORC diagrams provided additional constraints on the domain states and mineralogy of the magnetic particles (**Figure 4**). In general, closed contours in all the plots suggest that the magnetic particles exhibit vortex state to multidomain (MD) type behavior (Roberts et al., 2000; Roberts et al., 2017). FORCs indicate that the magnetic mineralogy of samples from MZ-1, MZ-2, and MZ-3

could be dominated by the ferrimagnetic iron oxides (Vortex state-MD type magnetite) and sulfides (SP Greigite) (**Figures 4A–G**) (Muxworthy and Dunlop, 2002). In all the samples, FORC distributions are characterized by a peak at coercive field $B_C \sim$ 10 mT with closed contours suggesting the dominance of vortex state behavior in magnetite (Lascu et al., 2018; Muxworthy and Dunlop, 2002; Roberts et al., 2017; **Figures 4A–I**). Greigite can exhibit both ultrafine-grained superparamagnetic (SP) (Rowan and Roberts, 2006; Rowan et al., 2009) and stable SD-type behavior (Roberts, 1995). Diagenetically reduced sediments enhances the formation of SP-size greigite particles (Tarduno, 1995; Rowan et al., 2009). Increase in SIRM/χ_{lf} in G1, G2 and G3 intervals confirms the presence of SP-sized greigite particles (**Figure 2E**; Maher and Thompson, 1999; Nowaczyk et al., 2012; Snowball and Thompson, 1990).

Low-Temperature Magnetic Measurements

Low-temperature magnetic measurements for representative samples selected from the different sediment magnetic zones MZ-1 (**Figure 5A**), MZ-2 (**Figure 5B**), MZ-3 (**Figure 5E**), G1 (**Figure 5C**), and G3 (**Figure 5D**) are presented. A well-developed Verwey (T_v 117–120 K) transition due to the presence of detrital magnetite is evident in RT-SIRM, ZFC-FC, and in the first derivative of magnetization curves (**Figures 5A,B,E**). During warming of RT-SIRM, remanence did not recover totally in these samples (MZ-1, MZ-2, and MZ-3) (Verwey, 1939;
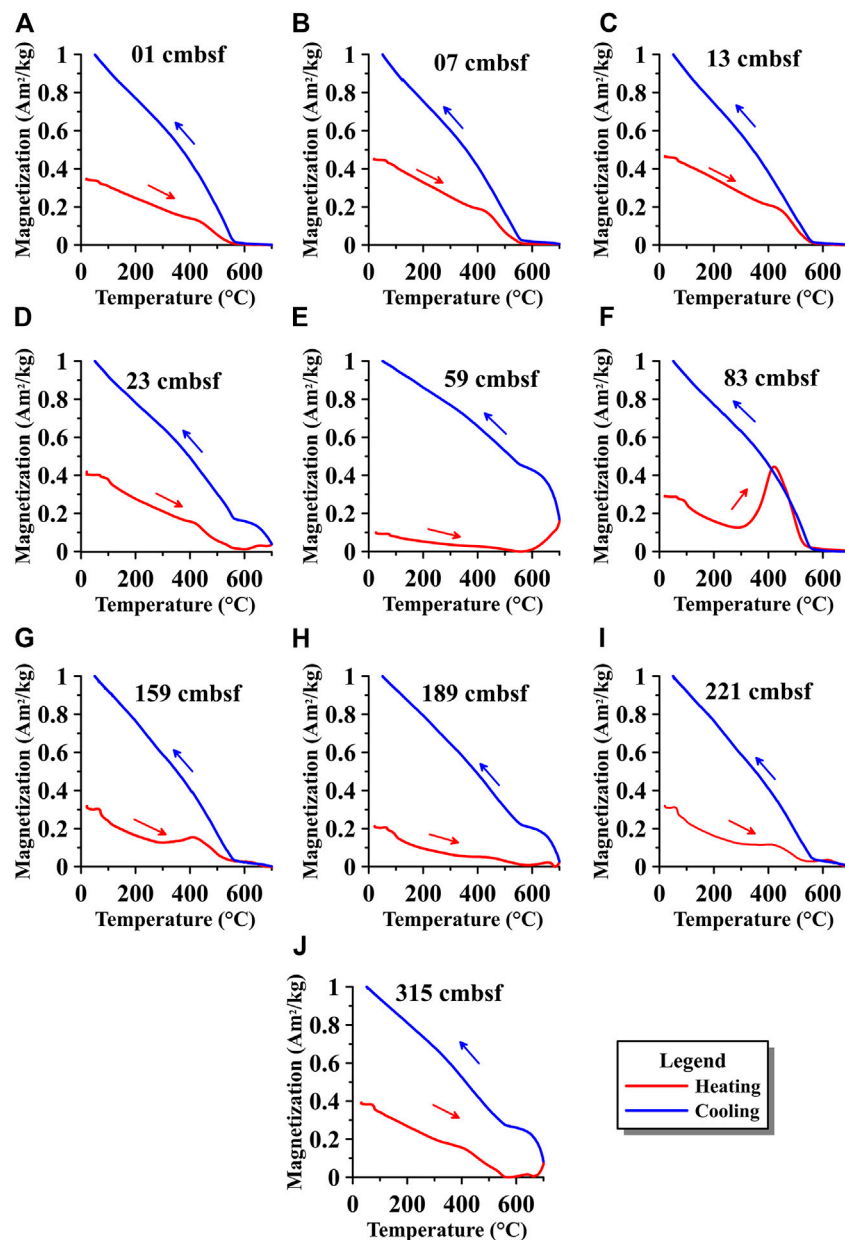
FIGURE 3 | (A–J) Thermomagnetic profiles of selected representative samples representing three sedimentary magnetic zones of the studied sediment core SSD-045/Stn-9/GC-01. Solid red lines indicate heating curves, and blue lines indicate cooling curves.

Muxworthy and McClelland, 2000; Özdemir et al., 2002; Chang et al., 2016). Samples (G1 and G3) from the zone of reduced magnetic susceptibility (MZ-2) did not show any indication of a Verwey transition in RT-SIRM, ZFC-FC, and the first derivative of magnetization curves (**Figures 5C**,D). We noticed that nearly 65% of the LT-SIRM imparted at 5K is lost during warming between 5 and 30 K (**Figures 5C**,D). This reflects the dominant presence of superparamagnetic (SP) magnetic particles in these samples (Tarduno et al., 1995; Passier and Dekkers, 2002). Kars and Kodama (2015) noticed a similar pattern of rapid decrease in LT-SIRM from 5 to ~30 K and ~50–60% loss of the imparted

remanence in the sediment samples from Magesplay fault Zone of the Nankai Trough, offshore Japan. They attributed that the loss of remanence was due to the presence of SP particles which get unblocked very rapidly. The SP magnetic particles in these samples (G1 and G3) are most likely iron sulfides like greigite or pyrrhotite. These can be explained by the fact that fine-grained magnetic particles in these samples would get readily dissolved in the sulfidic environment (as seen through lowest χ_{lf} in MZ-2). In contrast, the SP greigite nanoparticles are thermodynamically more stable compared to the SP magnetite nanoparticles and would rather remain preserved (Rowan et al., 2009; Roberts et al.,
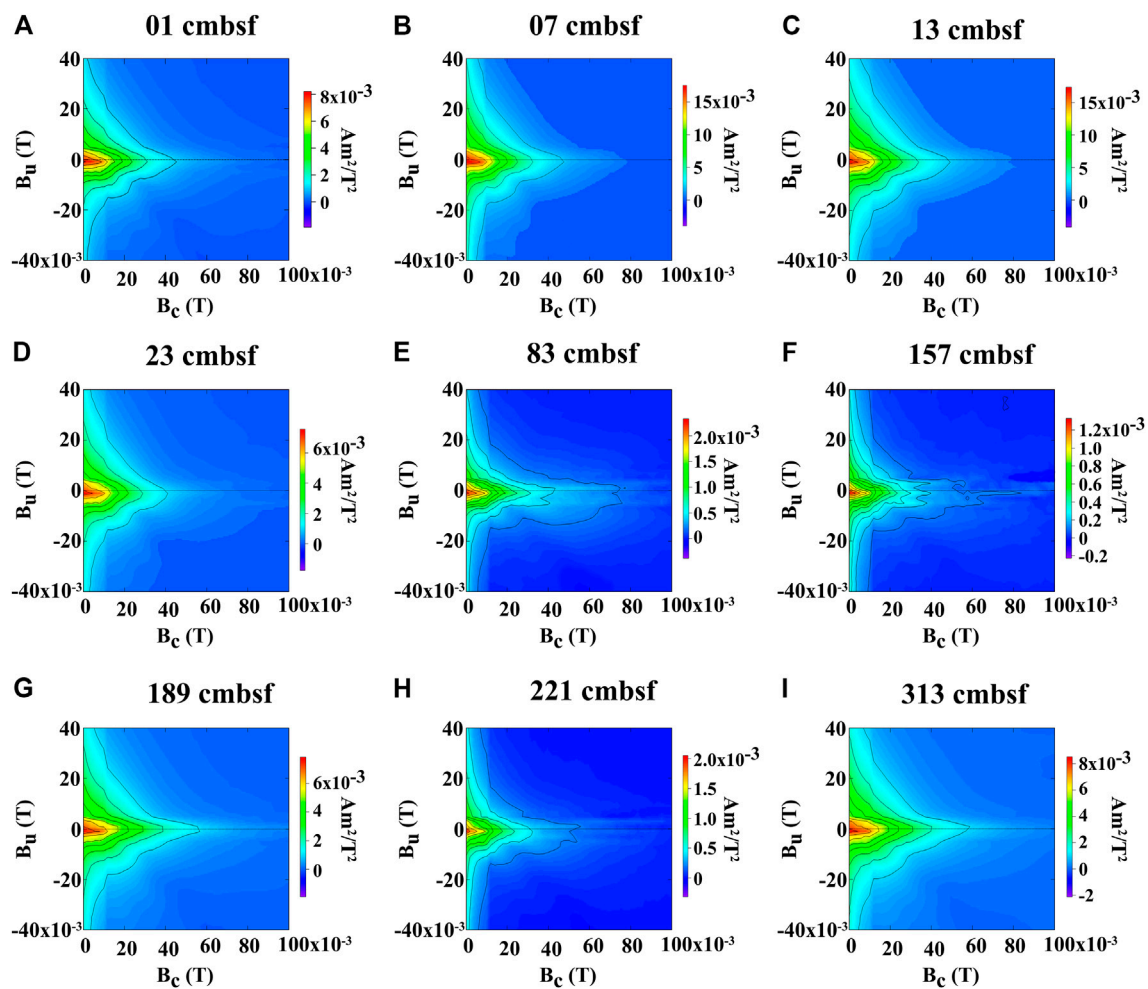
FIGURE 4 | (A–I) Representative first-order reversal curve diagrams for the three sedimentary magneto zones from core SSD-045/Stn-9/GC-01. All results are indicative of ferrimagnetic iron oxides, that is, titanomagnetite in the vortex state (Lascu et al., 2018; Roberts et al., 2017).

2018). Lack of LT transitions in the magnetization derivation curves in these samples (G1 and G3) is consistent and further confirms the presence of greigite (**Figures 5C**,D; Chang et al., 2009; Roberts et al., 2011).

Scanning Electron Microscope–Energy Dispersive X-ray Spectroscopy Observations of Magnetic Particles

In addition to rock magnetic parameters, SEM-EDS data confirm and support the interpretation on the magnetic mineralogy in core SSD-045/Stn-9/GC-01. Detrital origin ferrimagnetic iron oxides (titanomagnetite) of various sizes and shapes are found in all magnetic zones (**Figures 6A–L**). Magnetic zones (MZ-1, MZ-3) contain well-preserved titanomagnetite grains. EDS data for these grains indicate the presence of titanium, iron, and oxygen with minor amounts of calcium, silicon, aluminum, and manganese (**Figures 6B**,K,L).

Diagenetically formed iron sulfides are found to occur as sub-micron, spherical-shaped particles in MZ-1, MZ-2, G1, G2, and G3

(**Figures 6A,C,J**), and EDS spectra contain Fe and S peaks. Presence of such particles in the magnetic extracts from the zone of reduced χ_{lf} (G1, G2, G3) suggest that a ferrimagnetic iron sulfide i.e., greigite or pyrrhotite is the major constituent of the particles occurring as overgrowth on the paramagnetic host substrate such as pyrite (Rowan and Roberts, 2006). Sub-micron sized iron sulfide particles were also seen to occur as overgrowth on the large titanomagnetite grain in MZ-2 (**Figure 6E**). Several titanomagnetite grains of various sizes and shapes were found in the magnetically enhanced zone (MZ-3), and EDS spectra contain Ti, Fe, and O peaks (**Figures 6K,L**).

X-ray Diffraction (XRD) Analyses of Magnetic Minerals

Magnetic mineralogy is dominated by titanomagnetite, greigite, and pyrite particles occuring in varying proportion (**Figure 7**). XRD data confirms the dominant presence of pyrite along with minor peaks of greigite and titanomagnetite in G1, G2, and G3 (**Figures 7F**,I,K). Magnetically enhanced zone (MZ-3) contains titanomagnetite and pyrite (**Figures 7N,O**). Pyrite is the major

FIGURE 5 | (A–E) Low-temperature (<300 K) magnetization curves for representative samples from the three sedimentary magnetic zones identified in sediment core SSD-045/Stn-9/GC-01. FC, field-cooled; RTSIRM, saturation isothermal remanent magnetization at room temperature; ZFC, zero field-cooled.
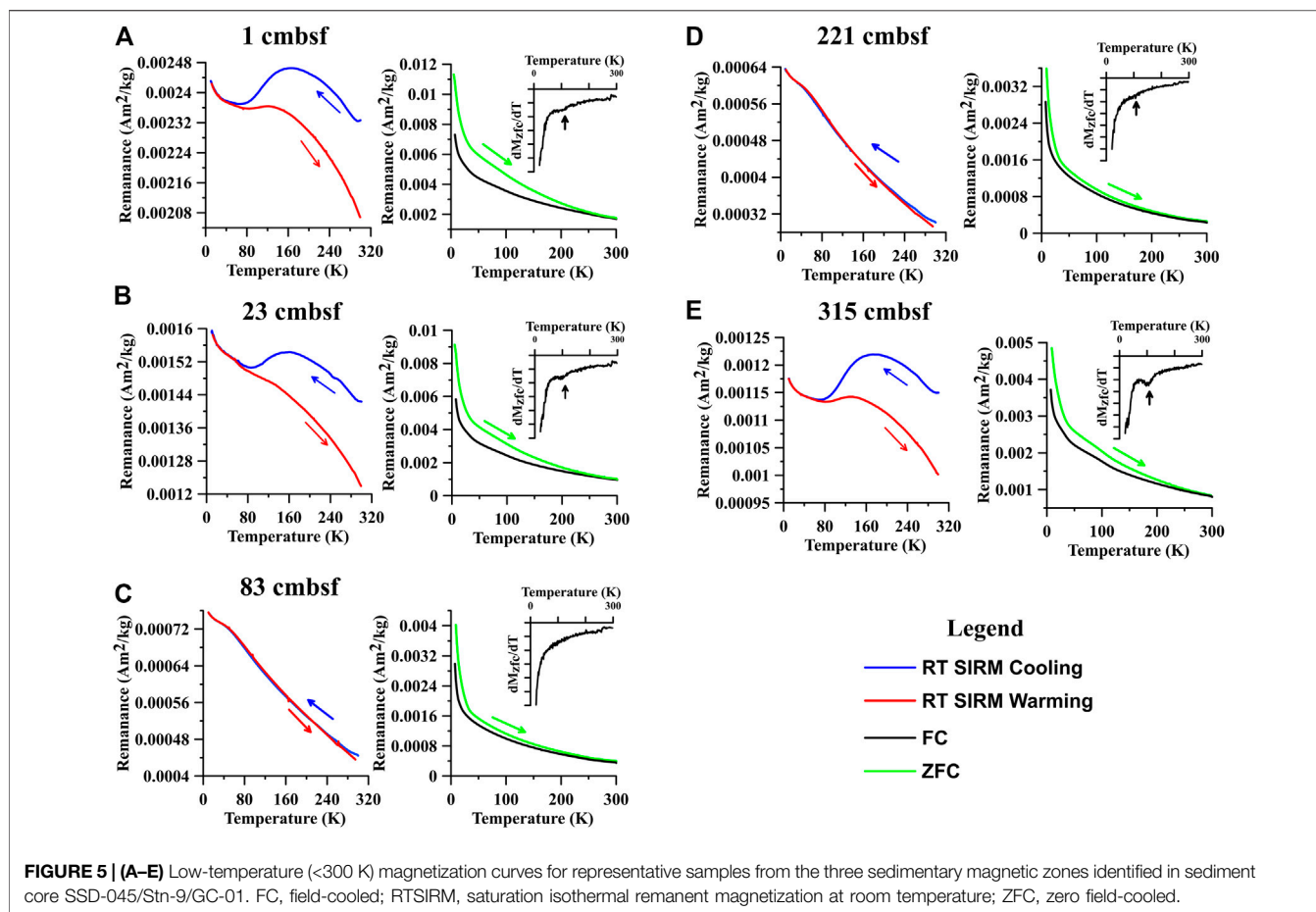
magnetic mineral in the zone of reduced χ_{lf} (MZ-2) (**Figures 7C–M**). XRD peaks corresponding to quartz are seen in all the samples (**Figure 7**).

Authigenic Carbonates and Chemosynthetic Clams

Gray color authigenic carbonates of various sizes and morphologies are found predominantly throughout the core. Representative images of the carbonates found within the greigite-bearing (G1, G2, G3) sediment intervals are presented in **Figures 8A–I**. Two relict shells of *Calyptogena* (family: Vesicomyidae) were found in the sediment depth intervals of 26–28 cmbsf and 50–52 cmbsf respectively (**Figures 8J,K; Table 1**).

Grain Size Distribution

Bulk sediment grain size in the core SSD-045/Stn-9/GC-01is dominated by the silt and clay sized fractions (**Figure 9**). Silt and clay content in this core varies from 14.56 to 52.29 vol% and 47.62–83.56 vol%, respectively. Down-core increase in sand content with distinct sediment intervals containing relatively higher sand concentrations at 83, 135, 197, 239, and 315 cmbsf are observed (**Figure 9**). Higher χ_{lf} were found in some of these

sand layers in MZ-1 and MZ-3 suggesting the presence of coarse-grained magnetic particles (**Figure 9**).

Correlation Between Magnetic Parameter and Mean Grain Size

A good correlation between χ_{lf} and SIRM is observed in all the samples, but exhibits differences in their slope suggesting the presence of ferri-and paramagnetic mineral assemblages in the samples (**Figure 10A**). A cross plot of SIRM/χ_{lf} vs. χ_{lf} has been successfully utilized as a proxy for characterizing the magnetic mineral assemblages in the gas hydrate bearing sediments (Larrasoaña et al., 2007; Kars and Kodama, 2015; Badesab et al., 2019). We broadly classify the samples into three sub-groups (**Figure 10B**). Samples exhibiting higher χ_{lf} and SIRM/χ_{lf} values suggest the presence of fine-grained magnetite. Higher values of SIRM/χ_{lf} and relatively low χ_{lf} in the majority of samples indicate the dominance of ferri-and paramagnetic iron sulfides. Samples which lies within the intermediate range of SIRM/χ_{lf} and χ_{lf} values represent the mixture of magnetic iron sulfides and magnetite (**Figure 10B**). A good covariation between χ_{lf} and mineralogy diagnostic S-ratio is seen (**Figure 10C**). Samples exhibiting low S-ratio and relatively narrow range in χ_{lf} can be attributed to the presence of either higher coercivity magnetic
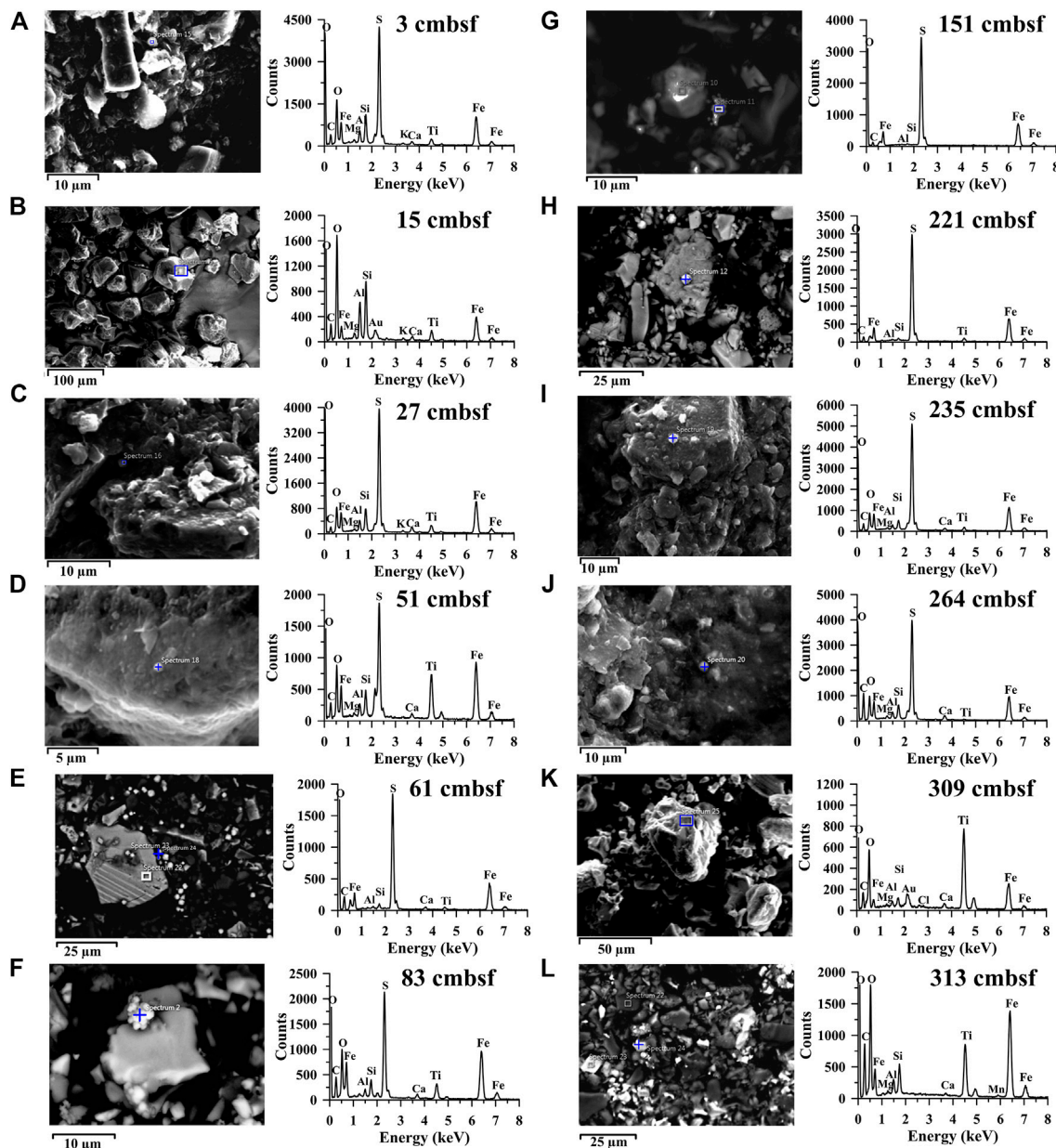
FIGURE 6 | (A–L) Scanning electron microscope images (secondary electron) on magnetic extracts from different sedimentary magnetic zones of core SSD045/Stn-9/GC-01. Energy dispersive X-ray spectroscopy spectra are placed adjacent to the respective images (A–L). Iron (Fe), titanium (Ti), sulfur (S), oxygen (O), calcium (Ca), silicon (Si), carbon (C), aluminum (Al), magnesium (Mg), and manganese (Mn) peaks are indicated.

minerals or ferrimagnetic iron sulfides (**Figure 10C**) (Peters and Dekkers, 2003; Roberts et al., 2011).

Mineralogy diagnostic rock magnetic parameters indicated that the bulk magnetic mineralogy is dominated by the vortex state titanomagnetite. Moskowitz et al. (1993) demonstrated that the origin of magnetic mineral assemblages in the sediment samples can be characterized by δ_{ZFC} and δ_{FC}. In the analyzed samples, we noticed that δ_{FC}/δ_{ZFC} values are close to 1, which

suggest that the titanomagnetites are of detrital origin (**Figure 10D**; Housen and Moskowitz, 2006). All data falls on a 1:1 line. Samples exhibiting low values δ_{ZFC} and δ_{FC} indicate the presence of diagenetically formed ferrimagnetic iron sulfides, while higher values of δ_{ZFC} and δ_{FC} indicates the presence of mixed-type (magnetite, pyrite) magnetic mineral assemblages (**Figure 10D**; Kars and Kodama, 2015; Badesab et al., 2019).
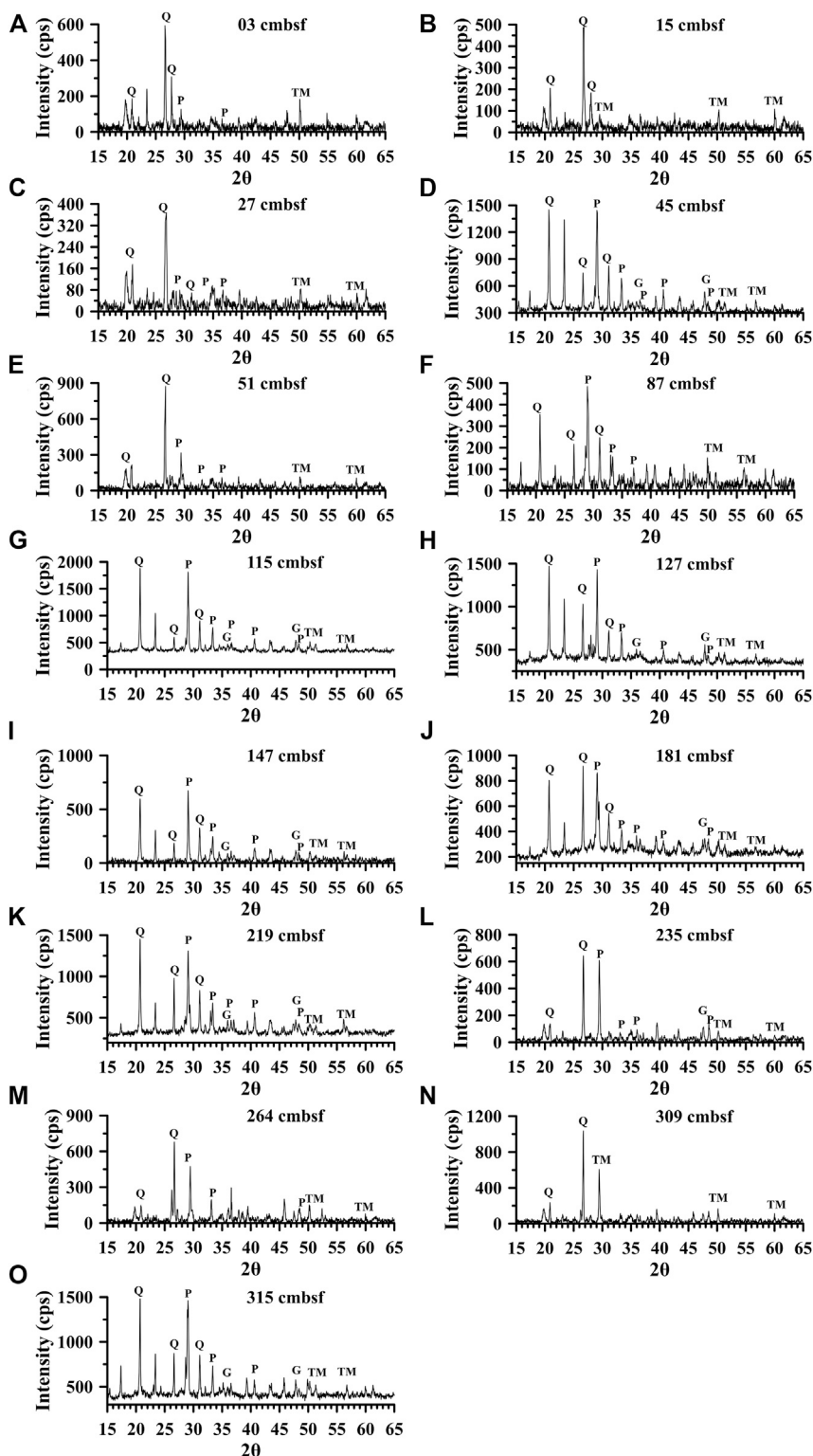
FIGURE 7 | (A–O) X-ray diffraction spectra for minerals extracted from different sedimentary magnetic zones of core SSD-045/Stn-9/GC-01 (a–o). TM, titanomagnetite; P, pyrite; Q, quartz; G, greigite.

FIGURE 8 | (A–I) Photographs showing methane-derived authigenic carbonates found in greigite bearing intervals (G1, G2, and G3) in MZ-2, **(J)** *Calyptogena* sp. showing growth layers identified at 27 cmbsf and **(K)** authigenic carbonate together with *Calyptogena* sp identified at 51 cmbsf.
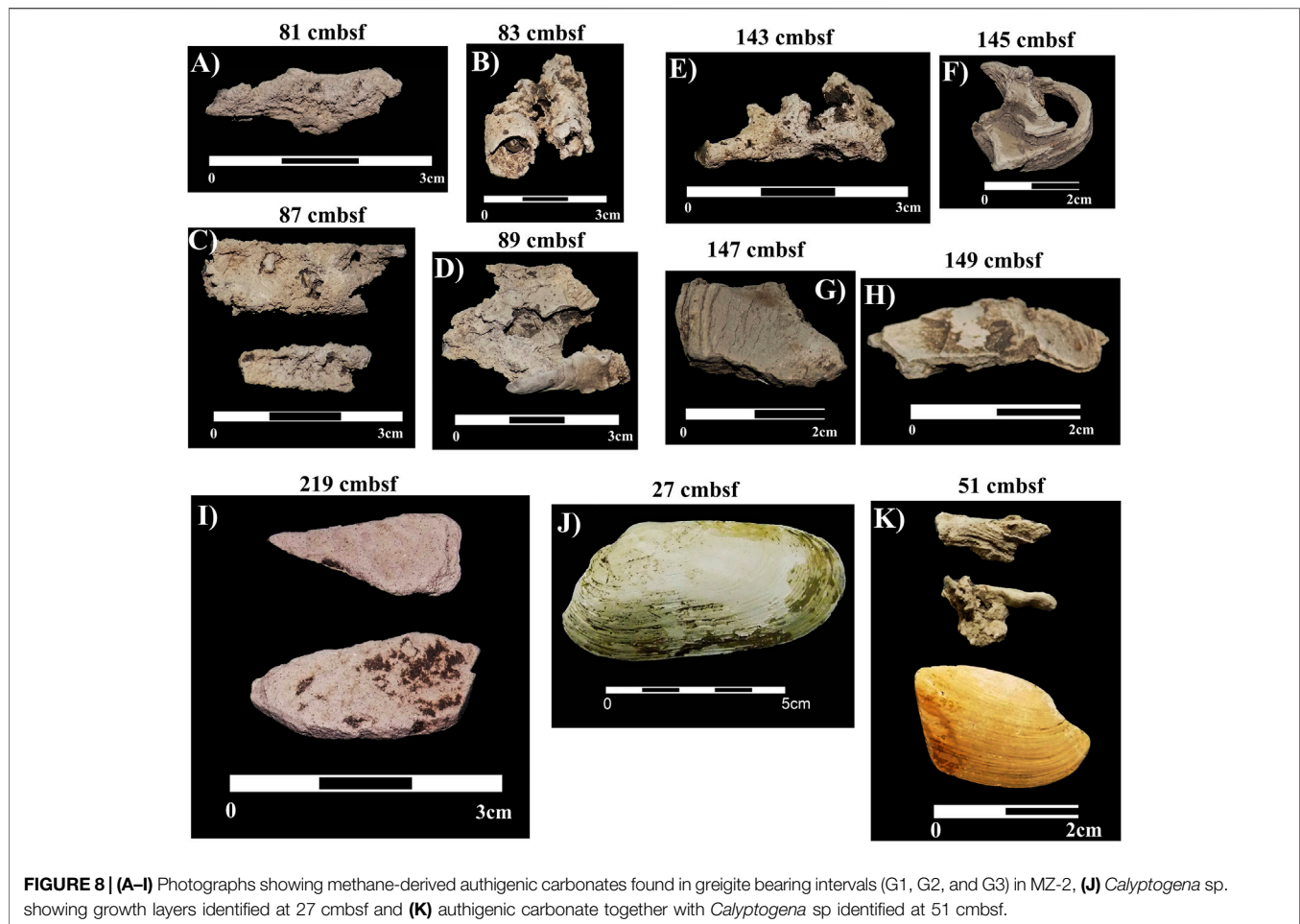
DISCUSSION

Paleo-Methane Seepage Events Constrained by Rock Magnetism, Authigenic Carbonates and Chemosynthetic Community

Variations in magnetic mineralogies (titanomagnetite, pyrite, greigite) and concentration governed the down-core changes in the magnetic properties. Primary magnetic minerals in the uppermost MZ-1 are dominated by titanomagnetite (vortex) with minor amount of pyrite (**Figures 2F**, **5A**, **6B**, **7A,B**). Gradual decrease of χ_{lf} in MZ-1 can be linked with the progressive dissolution of iron oxide and subsequent precipitation of iron sulfides. A distinct drop in χ_{lf}, ARM, and SIRM at the shallowest sediment interval (3–5 cmbsf) accompanied by the presence of pyrite and magnetite reflects the top-most dissolution front related to intense pyritization fueled by AOM-coupled sulfate reduction, and probably represent the depth of present-day SMTZ in the core SSD-045/Stn-9/GC-01 (**Figures 2A–C**, **6A**, **7A**). A systematic down-core increase in χ_{lf} and SIRM (from 7 to 17 cmbsf) manifested by the presence of magnetic particles below the proposed present-day SMTZ (3–5 cmbsf) indicate the period of weak AOM activity and minimum dissolution of the magnetic

minerals (**Figures 2A,C**, **6B**, **7A**). Rapid burial and preservation of the detrital magnetic particles due to increased sedimentation specifically during this period is another possibility (Badesab et al., 2019). A marked depletion in χ_{lf} between 25–29 cmbsf and 43–52 cmbsf reflects the periods of increased magnetite dissolution and pyrite formation linked with at least two intense methane seepage events at the studied site (**Figures 2A**, **6C,D**, **7C,E**). These intervals most likely reflect paleo-SMTZ front, where upward migrating methane front interact with downward migrating sulfate front to trigger strong AOM.

The AOM increases the concentration of hydrogen sulfide in the pore-water and favor dissolution of primary magnetic mineral assemblages (Kasten et al., 1998; Jørgensen et al., 2004; Dewangan et al., 2013). Similar low χ_{lf} intervals due to paleo-methane expulsion events were reported from the K-G basin and South China Sea (Mazumdar et al., 2009; Peketi et al., 2012; Dewangan et al., 2013; Hu et al., 2019). The presence of chemosynthetic clams like *Callyptogena* sp. and methane derived authigenic carbonates provided further evidences of intense methane seepage events at these sediment intervals (**Figures 2A**, **6C,D**, **7C–E**, **8J**,K; **Table 1**). Fossil chemosynthetic community and authigenic carbonates were reported from site MD161/Stn-8 and NGHP-01–10D in K-G basin (Collett et al., 2008; Mazumdar et al., 2009, Peketi et al., 2012), Haima Seep, South China Sea

Sr. No.	Authigenic carbonates ref. no.	Depth (cmbsf)	Other details
1	—	27	Shells
2	AGC-01	45	—
3	AGC-02	49	—
4	AGC-03	51	Shells + AGC
5	AGC-04	53	—
6	AGC-05	55	—
7	AGC-06	57	—
8	AGC-07	59	—
9	AGC-08	61	—
10	AGC-09	63	—
11	AGC-10	65	—
12	AGC-11	67	—
13	AGC-12	69	—
14	AGC-13	71	—
15	AGC-14	73	—
16	AGC-15	75	—
17	AGC-16	77	—
18	AGC-17	79	—
19	AGC-18	81	—
20	AGC-19	83	—
21	AGC-20	87	—
22	AGC-21	89	—
23	AGC-22	91	—
24	AGC-23	93	—
25	AGC-24	95	—
26	AGC-25	99	—
27	AGC-26	101	—
28	AGC-27	103	—
29	AGC-28	105	—
30	AGC-29	107	—
31	AGC-30	111	—
32	AGC-31	113	—
33	AGC-32	115	—
34	AGC-33	117	—
35	AGC-34	119	—
36	AGC-35	121	—
37	AGC-36	123	—
38	AGC-37	137	—
39	AGC-38	139	—
40	AGC-39	141	—
41	AGC-40	143	—
42	AGC-41	145	—
43	AGC-42	147	—
44	AGC-43	149	—
45	AGC-44	197	—
46	AGC-45	219	—

(Feng and Chen 2015; Liang et al., 2017), southwest Barents and Norwegian Sea (Crémière et al., 2016), Mediterranean Sea (Aloisi et al., 2000), and Gulf of Mexico (Bian et al., 2013). Downward decrease in ARM/SIRM (9–19 cmbsf in MZ-1) is followed by the consistent low χ_{lf} and ARM/SIRM values in MZ-2 (25–265 cmbsf; **Figures 2A**,D). As confirmed through the XRD (**Figures 7C–M**) and SEM-EDS (**Figures 6F**,H), the dominant magnetic mineral in MZ-2 is titanomagnetite (vortex) and pyrite. It is most likely that fine SD magnetite grains might have been preferentially removed by diagenetic dissolution (**Figures 2A–D**) owing to larger surface area (Karlin and Levi, 1983; Liu et al., 2004; Garming et al., 2005). The dominance of pyrite and titanomagnetite within

59–265 cmbsf interval of MZ-2 coupled with abundant occurrence of authigenic carbonates suggest that the strong SMTZ fronts sustained due to uniform supply of methane gas from the deep-seated reservoir (**Figures 2A, 6E–H,J, 7F–M**). It is interesting to note that a lower S-ratio interval (229–241 cmbsf) is observed in MZ-2. Horng, C.S. (2018) and Kars and Kodama (2015) reported that sedimentary pyrrhotite and greigite can have high coercivities which could result in low S-ratio. A dedicated rock-magnetic study conducted by Kars and Kodama (2015) on gas hydrate bearing sediments from Nankai trough reported that authigenically formed ferrimagnetic iron sulfides such as greigite
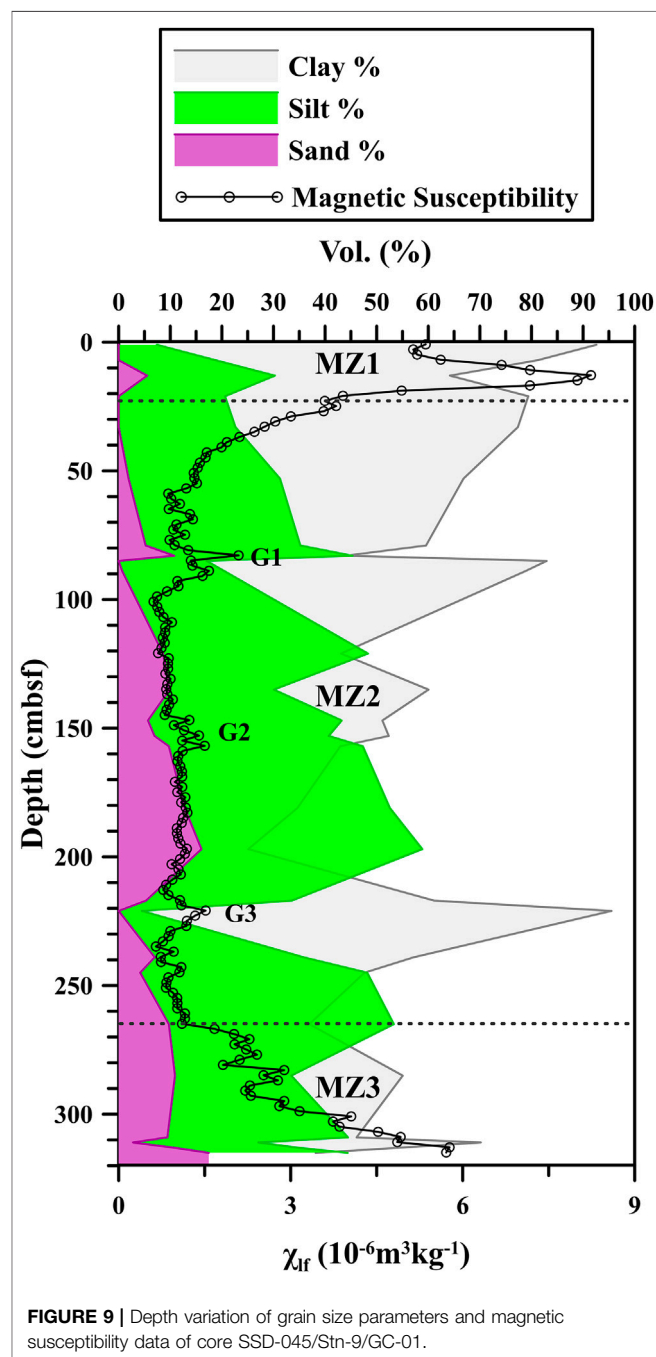
FIGURE 9 | Depth variation of grain size parameters and magnetic susceptibility data of core SSD-045/Stn-9/GC-01.
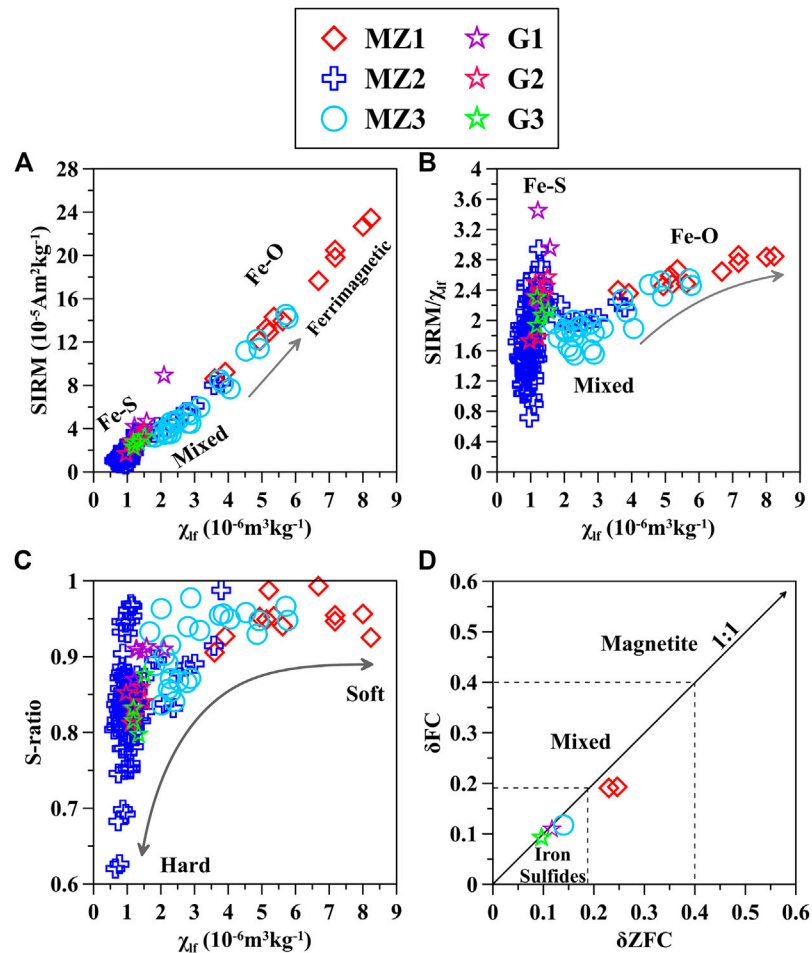
FIGURE 10 | (A–C) Scatterplots of magnetic parameters χ_{lf}, saturation isothermal remanent magnetization (SIRM), SIRM/χ, anhysteretic remanent magnetization (ARM)/SIRM, and S- for core SSD-045/Stn-9/GC-01. **(D)** δFC vs. δFC are derived from low-temperature measurements (Moskowitz et al., 1993) for core SSD-045/Stn-9/GC-01. Please note that gray color arrows in the scatter plots are used to highlight trends.

and pyrrhotite can exhibit high coercivities. The lower S-ratio interval observed in MZ-2 could be attributed to the presence of such ferrimagnetic iron sulfides (greigite/pyrrhotite) which were no longer stable and got converted into pyrite as evident through low χ_{lf} within 209–231 cmbsf, (**Figure 2A**) and SEM-EDS data (**Figures 6H,I**).

Lowermost sediment magnetic zone (MZ-3) is characterized by elevated χ_{lf}, ARM, SIRM, and contains the mixture of abundant detrital titanomagnetites and minor amount of diagenetically formed pyrite (**Figures 2A–C, 5E, 6K,L, 7N,O**). High χ_{lf} accompanied by mixed trend of ARM/SIRM values could be attributed to the presence of both fine and coarse-grained detrital magnetic particle which probably survived diagenesis (**Figures 2A**,D). Fracture-filled gas hydrates deposits were recovered from MZ-3 (305–315 cmbsf, **Figure 1B**). Trapping of H$_2$S within the hydrate deposits hindered the pyritization processes (Housen and Musgrave, 1996), and lead to the preservation of detrital magnetite particles in MZ-3 (Riedinger et al., 2005) (**Figures 2A, 4I, 5E, 6K,L, 7N,O**). Rapid burial of magnetic particles is another important factor which can explain

the existence of high χ_{lf} in gas hydrate bearing sediments (Badesab et al., 2019). We believe that both these processes hindered the diagenetic reactions and favored high χ_{lf} values in the gas hydrate bearing sediments at site Stn-9.

A dedicated magnetic study on pelagic sediments from western equatorial Pacific Ocean revealed that diagenetically reduced sediments could enhance the formation of SP-size greigite particles (Tarduno, 1995). Increase in SIRM/χ_{lf} in G1, G2, G3 intervals confirms the presence of SP-sized greigite particles (**Figure 2E**; Tarduno, 1995). FORC distributions from the same greigite bearing samples G1, G2 and G3 also showed closed contours indicative of vortex-type magnetic behavior (**Figures 4A–I**; Lascu et al., 2018; Muxworthy and Dunlop, 2002; Roberts et al., 2017). These observations suggests that magnetic particles in G1, G2, G3 and MZ-3 (313 cmbsf) in core SSD-045/Stn-9/GC-01 is dominated by SP greigite and vortex-state magnetite. Hence the minor rise in SIRM/χ_{lf} (**Figure 2E**) manifested by the presence of pyrite (**Figure 7O**) in MZ-3 (301–315 cmbsf) can be explained by the fact that ferrimagnetic greigite which was formed earlier

might have got transformed into more stable pyrite (Larrasoaña et al., 2007; Kars and Kodama 2015).

Occurrence of active methane seep are often associated with shallow gas hydrates and presence of seep-carbonates and has been well documented worldwide; for example offshore southwest Africa, Congo deep sea fan (Pierre and Fouquet, 2007), eastern Mediterranean Sea (Aloisi et al., 2000), northern Apennines and Tertiary Piedmont Basin of Italy (Dela Pierre et al., 2010; Argentino et al., 2019), Nyegga complex pockmark, Norwegian Sea (Mazzini et al., 2006), South China Sea (Tong et al., 2013; Han et al., 2014), Blake Ridge Diapir (Naehr et al., 2000), and Vestnesa Ridge, NW Svalbard (Schneider et al., 2018). At active seeps, methane gets consumed and this process generates dissolved bicarbonate, thereby increasing porewater alkalinity and favors precipitation of authigenic carbonate close to the seafloor (Boetius et al., 2000). Thus, the authigenically formed carbonates are considered as potential archives of past fluid flow (Aharon et al., 1997; Bayon et al., 2013; Feng and Chen, 2015). Repeated occurences of authigenic carbonates (**Figures 8A–K**; **Table 1**) from 45 to 219 cmbsf in core SSD-045/Stn-9/GC-01 indicate the episodic events of intense AOM due to enhanced methane flux. This also show the variability in past methane fluxes could be due to episodic ventilation of deep-seated methane gas or dissociation of gas hydrates or opening/closing of fault/fracture system driven by neo-tectonic activity (Dewangan et al., 2020).

Association of chemosynthetic communities with methane seepage has been reported from several cold seep locations (Sellanes and Krylova, 2005; Levin et al., 2016; Amon et al., 2017; Mazumdar et al., 2018). Evidence for the strong methane seepage events at 25–29 cmbsf and 43–52 cmbsf, and subsequently anaerobic oxidation of methane comes from the occurrence of authigenic carbonate nodules, chemosynthetic communities (*Calyptogena* sp.), and pyrite followed by distinct χ_{lf} drop at this intervals (**Figures 2A**, **8J**,K). Similar observations were reported from site MD161/Stn-8 in the K-G basin (Mazumdar et al., 2009; Dewangan et al., 2013). Variations of methane fluxes at seeps determine the migration of the SMTZ in marine sediments (Borowski et al., 1996). Delineation of SMTZ and the factors controlling its migration in a seep-impacted sediments could help in tracking the evolution of past methane seepage events. Previous studies employed various proxies to recognize the SMTZ and detect the past methane seepage events including Ba front (Dickens, 2001; Snyder et al., 2007), methane-derived authigenic carbonates, mineralogy and its carbon isotope composition (Teichert and Luppold, 2013; Kocherla et al., 2015), Sulfur isotope and Mo anomaly (Peketi et al., 2012) and magnetic susceptibility (Badesab et al., 2019). Fluctuations in methane fluxes in a complex gas hydrate bearing marine sedimentary system can also be tracked successfully using χ_{lf} records, for examples in K-G basin (Badesab et al., 2019; Dewangan et al., 2013; Usapkar et al., 2014), the Argentine continental slope (Garming et al., 2005), Nankai trough, Japan (Kars and Kodama, 2015), and Cascadia margin (Housen and Musgrave, 1996; Larrasoaña et al., 2007). Rock magnetic record of core SSD-045/Stn-9/GC-01 provides evidence of rapid SMTZ migration controlled

by changing methane fluxes. Mineralogical analyses on the core revealed the presence of abundant diagenetically formed pyrite and minor amount of titanomagnetite within the zone (MZ-2) of reduced χ_{lf} (**Figures 7D–M**). Such phenomena can be attributed to the reducing environment associated with upward methane flux which enhances diagenesis of the highly magnetic detrital minerals such as titano-magnetite into nearly non-magnetic pyrite (Housen and Musgrave, 1996). In zone of reduced susceptibility (MZ-2), multiple episodes of seepage activities controlled the diagenetic alteration of magnetic minerals and hence have a direct impact on χ_{lf}. However, tracking paleo-SMTZ fronts can be challenging at times due to the differences in the rate of diagenesis constrained by changing methane fluxes. In such a scenario, the occurrence of authigenic carbonates would be useful in delineating the paleo-methane seepage activities. The abundant occurrence of authigenic carbonates in a depth range from 45 to 219 cmbsf within MZ-2 suggests that the SMTZ was quite variable in the past (**Figures 8A–I**; **Table 1**). We demonstrate that combination of rock magnetic and mineralogical (SEM-EDS, XRD) data together with authigenic carbonates are useful to identify the present and past SMTZ fronts fueled by methane seepages.

Possible Linkage Between Greigite Precipitation, Neo-Tectonic Events and Formation of Gas Hydrates (Disseminated-Type vs. Massive) in the Krishna-Godavari Basin

Fracture-controlled fluid migration has been well-reported at cold seeps, for example in Vestnesa Ridge (Yao et al., 2019), Harstad Basin, southwest Barents Sea (Vadakkepuliyambatta et al., 2013; Crémière et al., 2018), Hydrate Ridge (Torres et al., 2002; Weinberger and Brown, 2006), Blake Ridge (Egeberg and Dickens, 1999), and Central Chile (Geersen et al., 2016). Fractures/faults facilitate efficient transport of methane-rich fluids from greater depth to shallower depth, and sometimes methane escape from sediment-water interface as flares (Berndt et al., 2014; Sahling et al., 2014). In methanic sediments, interplay between availability of reactive iron supply and relative production of hydrogen sulfide (HS−) control the pyritization process (Wilkin and Barnes, 1997). In case of excess HS− and high availability of reactive iron, the pyritization process is complete and the metastable iron sulfides are eventually converted to pyrite (Berner, 1967). Under low HS− concentration greigite may preferentially be precipitated over pyrite and will lead to the preservation of greigite. Migration of methane-rich fluids is found to be associated with the authigenic ferrimagnetic iron sulfide minerals like greigite and/or pyrrhotite (Larrasoaña et al., 2007). Greigite formation is enhanced in the vicinity of gas hydrate deposits as observed in Hydrate Ridge (Larrasoaña et al., 2007) and Blake Ridge (Wellsbury et al., 2000). For greigite formation and preservation, either limited amount of hydrogen sulfide or increased supply of reactive iron is required to constrain the pyritization process in methanic sediments (Liu et al., 2004). For example, Kao et al., 2004 demonstrated that

widespread greigite preservation is likely if abundant reactive iron is available to react with sulfide during pyritization reactions. Roberts et al., 2011 suggested that the preservation of greigite depends on the balance between sulfide production and reactive iron concentration. In the studied core, three distinct greigite (G1, G2, and G3) bearing sediment intervals (81–93 cmbsf, 145–159 cmbsf, and 217–229 cmbsf) has been identified within the zone of reduced χ_{lf}. Presence of greigite has been further confirmed through rock magnetic (χ_{lf} and SIRM/χ_{lf}), SEM-EDS and XRD (**Figures 2A,E**, **6F–H**, **7I–K**). A general trend of downcore increase in magnetic grain size diagnostic proxy (ARM/SIRM) in MZ-2 is observed (**Figure 2D**; Maher and Thompson, 1999). ARM/IRM first decreases in MZ-1 because of preferential dissolution of fine-grained magnetite (Maher, 1988) in the upper part of the reduced zone, and rises downcore in response to the formation of fine-grained greigite in MZ-2. A rockmagnetic study conducted on a sediment core from Niger deep-sea fan by Dillon and Bleil (2006) observed that the iron redox boundary is very shallow (~3 mbsf) and below, a pervasive magnetite dissolution has taken place. Similar to our observations, they noticed minor increase in ARM/SIRM with depth after an initial drop. They attributed the steadily increasing ARM/SIRM ratio in the anoxic sulfidic zone with the small gradually growing SD fraction of magnetic sulfides, for example authigenic formation of greigite is most likely in such environment and similarly reported in Mediterranean sapropels (Roberts et al., 1999; Passier and Dekkers, 2002) and Korean Strait (Liu et al., 2004). Increase in SIRM/χ_{lf} in G1, G2 and G3 intervals also suggest the presence of authigenically formed SP-sized greigite particles in the studied core (**Figure 2E**). Within the zone of reduced χ_{lf} (MZ-2), elevated methane concentration might have allowed huge production of sulfide which enabled complete pyritization and restricted the greigite preservation as seen through lower and uniform values of χ_{lf}, SIRM and abundant presence of pyrite in MZ-2 (**Figures 2A,C, 7C–M**). In contrast, decline in methane flux at G1, G2, and G3 intervals probably generated less sulfide, and favored the formation and preservation of greigite. Similar observation was made by Dewangan et al., 2013, where the presence of a thick authigenic carbonate layer beneath the SMTZ at site MD161/Stn-08 in K-G basin (Mazumdar et al., 2009) hindered the downward diffusion of sulfide favoring early arrest of the pyritization process and preservation of greigite. At the present site, low methane flux might have supported more distributed-type (vein-filling) hydrate deposits instead of massive deposits formed due to enhanced methane flux. We, therefore, propose that these three greigite bearing sediment intervals (G1, G2, and G3) are associated with distributed-type gas hydrate intervals at site Stn-9. However, we do not completely rule out the possibility of greigite formation due to increase in iron content in G1, G2, and G3.

A linkage between occurrence of greigite and increased clay content is evident (**Figure 9**). We propose a following plausible mechanism to explain the linkages between methane migration and formation of distributed-type (vein-filling gas hydrates), grain size and greigite formation and preservation. High resolution X-ray investigation conducted on the gas hydrates recovered from K-G basin revealed that hydraulic fractures created by upward migrating fluids was the dominant mechanism for the formation of veined-hydrate deposits at site NGHP-01–10 (Rees et al., 2011). At site Stn-9, it is highly possible that rapid migration of diffusive methane flux through the clay rich intervals in G1, G2, and G3 probably created multiple hydro-fractures which provided conducive environment for the formation of distributed–type (vein-filling) hydrates in these intervals. Growth of vein-filling hydrate network trapped the available sulfide within it and created a closed system by forming an impermeable layer which further restricted the supply of the downward diffusing sulfate (sea water) through the hydrate-bearing interval. A sulfide deficient zone is created which caused arrestation of pyritization and favored formation and preservation of greigite in G1, G2, and G3. Geochemical study conducted by Kao et al. (2004) on sediment cores from southwestern Taiwan reported that detrital minerals will survive in sediments if the methane fluxes are too small. At the studied site, fracture-filled gas hydrates were recovered from MZ-3 (305–315 cmbsf). Survival of detrital titanomagnetite particles in MZ-3 could be explained based on the fact that the lower methane (free) concentration in these intervals due to the presence of massive gas hydrate beneath this interval might have restricted the further diagenetic transformation of iron oxides into iron sulfides.

Grain size also provides important control on the gas hydrate formation in marine sedimentary system (Clennell et al., 1999; Torres et al., 2008). In Blake Ridge, high methane hydrate concentrations were found in sediment layers containing high silt content (Ginsburg et al., 2000; Lorenson, 2000). Overall, clay and silt dominate the bulk sediment grain size in the studied core (**Figure 9**). Marked peaks of decrease in silt content and concurrent rise in clay content more specifically within gas hydrate bearing intervals (G1, G2, G3 and bottom most: 305–315 cmbsf) suggest that distributed methane hydrate accumulation in veins/fracture preferentially occurs in the sediment intervals containing high clay content (**Figures 2A, 9**).

Regulation of gas plumbing system due to opening/closing of the fractures/faults provides important constraints on the methane flux (Dewangan et al., 2011; Sriram et al., 2013; Mazumdar et al., 2019). Widespread occurrence (45–219 cmbsf) of authigenic carbonates in the studied core suggests that the multiple AOM driven by variability in paleo-methane fluxes is controlled by the opening and closing dynamics of the fracture/fault system due to prevailing shale tectonism (Dewangan et al., 2010; Gullapalli et al., 2019; Mazumdar et al., 2019). Sahling et al. (2014) also suggested that micro and macro fractures are often found associated with cold seep systems, wherein methane from deep-seated reservoir moves upward to sediment-water interface such as Hydrate Ridge (Torres et al., 2002) and Blake Ridge (Egeberg and Dickens 1999). At site Stn-9, fracture-controlled fluid transport supported the formation of gas hydrates (distributed and massive-type) (Mazumdar et al., 2019). We believe that hydrate crystallizes within the fault/fractures zone as methane gas migrate through GHSZ (You et al., 2019). It is interesting to note that several layers of hard authigenic carbonates are found above and within the proposed

FIGURE 11 | Conceptual model explaining the mechanism controlling the shallow gas hydrate formation, greigite preservation and development of active cold seep system in the K-G basin.
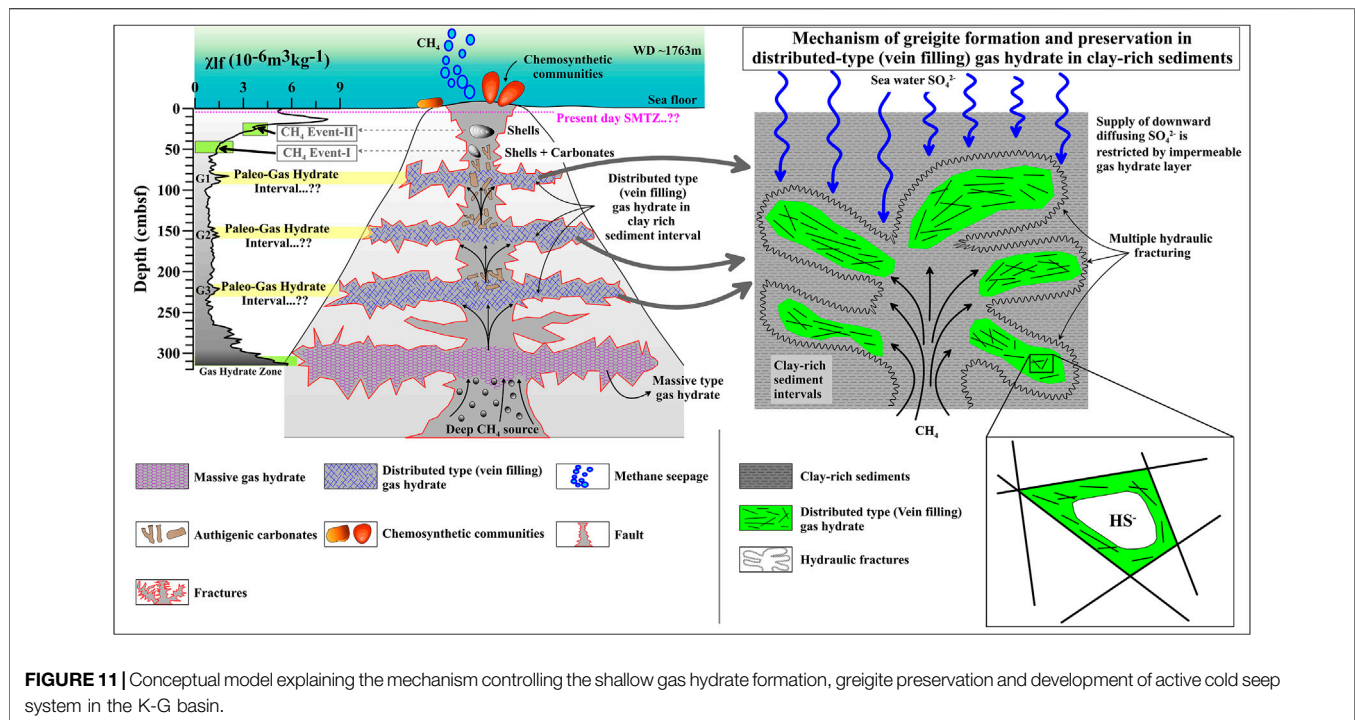
distributed-type gas hydrate bearing intervals (G1, G2, G2) (**Table 1**). It may also be possible that formation of authigenic carbonate layers coupled with clay deposits restricted the upward migrating methane and led to the formation of distributed-type hydrate deposits. The distributed gas hydrate deposits build a closed system, which prevented the completion of pyritization process and thus, favored the formation and preservation of SP size greigite.

Evolution of Active Cold Seep System in Krishna-Godavari Basin: Constraints From Rock Magnetic, Microscopy and Mineralogical Proxies

We propose a plausible mechanism to explain the various features of an active cold seep system associated with shallow gas hydrates in the K-G basin (**Figure 11**). At active seep site, early diagenesis of magnetic minerals occurs very close to the sediment-water interface resulting in dissolution of primary detrital iron oxides and subsequent conversion to iron sulfides (pyrite). Distinct drop in concentration-dependent magnetic parameters manifested by the presence of diagenetically formed pyrite between 3 - 5 cmbsf represent the top-most dissolution front (recent) and can be attributed to the intense pyritization fueled by AOM-coupled sulfate reduction and probably represent the depth of present-day SMTZ in core SSD-045/Stn-9/GC-01. A couple of sediment intervals (25–29 cmbsf and 43–52 cmbsf) also show marked depletion in magnetic susceptibility and abundant presence of pyrite grains suggesting at least two events of huge H_2S build up by intense methane seepage events. Presence of chemosynthetic shells (*Calyptogena* Sp.), authigenic carbonates at these intervals confirm the paleo-methane seepage at site Stn-9. The existence of low and uniform magnetic susceptibility in MZ-2 (except G1, G2,

and G3) reflects intense reductive diagenesis fueled by the elevated methane supply, which allowed the production of large concentration of sulfide, and led to transformation of primary iron-bearing magnetic minerals into paramagnetic pyrite. Repeated occurences of authigenic carbonates from 45 to 219 cmbsf in core SSD-045/Stn-9/GC-01 support multiple episodes of AOM intensification in the past. The opening/ closing of fault/fractures due to neo-tectonic activities allowed migration of methane from deep-seated gas reservoir (Dewangan et al., 2011; Sriram et al., 2013; Dewangan et al., 2020; Mazumdar et al., 2019). Upon entering the shallow depths and encountering conducive P-T conditions, gas hydrates started crystallizing within the faults and fractures where methane concentration exceeded the solubility limit (You et al., 2019). We propose that the distributed-type gas hydrate formed in veins during periods of reduced methane flux at clay rich intervals (G1, G2, G3) arrested the pyritization process and favored the preservation of the intermediate iron sulfides minerals (greigite/pyrrhotite) (Larrasoaña et al., 2007).

High magnetic susceptibility in the bottom most sediment interval containing massive gas hydrate deposit (MZ-3) can be attributed to the survival of detrital magnetic grains due to both hinderance of diagenetic reactions due to trapping of H_2S within hydrate (Housen and Musgrave, 1996; Riedinger et al., 2005) and rapid burial and preservation of the detrital magnetic grains due to higher sedimentation events (Badesab et al., 2019). Such gas hydrates requires efficient methane migration from deep-seated reservoir through the fracture system as evident from the existence of seismic chimneys beneath this site (Dewangan et al., 2020). Some active faults may even transport methane to seafloor, which is observed as methane gas flares (Mazumdar et al., 2019).

CONCLUSION

Rock magnetic, sedimentological and mineralogical record of the sediment core SSD-045/Stn-9/GC-01 retrieved from a newly discovered active methane seep site in the K-G basin provided important constraints on the evolution of past methane seepage dynamics and gas hydrate formation over geologic time. Two events of intense methane seepage were identified in the studied core. Occurences of several layers of authigenic carbonates throughout the core followed by the presence of chemosynthetic shells (*Calyptogena* Sp.) at two distinct sediment depth intervals provided clues on the episodic intensification of AOM at the studied site. Three greigite bearing sediment intervals within the magnetically reduced sulfidic zone reflect the paleo-gas hydrate (distributed-type vein filling) intervals in the studied core. A linkage between increase clay content, formation of veined hydrate deposits, precipitation of authigenic carbonates and greigite preservation is evident. Our findings are summarized into a conceptual model (**Figure 11**) which explains the controls on the magnetic mineral diagenesis, methane seepage dynamics, and the evolution of shallow gas hydrate (distributed vein filling vs. massive-type) system in the K-G basin.

DATA AVAILABILITY STATEMENT

The datasets presented in this study can be found in online repositories. The names of the repository/repositories and accession number(s) can be found below: https://publication-data.nio.org/s/9DdiMtsnJGG7dTQ.

AUTHOR CONTRIBUTIONS

FB and PD developed the concept for the manuscript. PD and VG have contributed toward sediment core collection and sampling during the research expedition (SSD-045) onboard R/V Sindhu Sadhana. Analyses were performed by VG and FB. All authors contributed equally to the writing and editing of the manuscript and preparation of figures and table.

FUNDING

ACKNOWLEDGMENTS

REFERENCES

Aharon, P., Schwarcz, H. P., and Roberts, H. H. (1997). Radiometric dating of submarine hydrocarbon seeps in the Gulf of Mexico. *Geol. Soc. Am. Bull.* 109 (5), 568–579. doi:10.1130/0016-7606(1997)109<0568:RDOSHS>2.3.CO;2

Aloisi, G., Pierre, C., Rouchy, J. M., Foucher, J. P., and Woodside, J. (2000). Methane-related authigenic carbonates of eastern Mediterranean Sea mud volcanoes and their possible relation to gas hydrate destabilisation. *Earth Planet. Sci. Lett.* 184 (1), 321–338. doi:10.1016/S0012-821X(00)00322-8

Amon, D. J., Gobin, J., Van Dover, C. L., Levin, L. A., Marsh, L., and Raineault, N. A. (2017). Characterization of methane-seep communities in a deep-sea area designated for oil and natural gas exploitation off Trinidad and Tobago. *Front. Mar. Sci.* 4, 342. doi:10.3389/fmars.2017.00342

Argentino, C., Lugli, F., Cipriani, A., Conti, S., and Fontana, D. (2019). A deep fluid source of radiogenic Sr and highly dynamic seepage conditions recorded in Miocene seep carbonates of the northern Apennines (Italy). *Chem. Geol.* 522, 135–147. doi:10.1016/j.chemgeo.2019.05.029

Badesab, F., Dewangan, P., Gaikwad, V., Kars, M., Kocherla, M., Krishna, K. S., et al. (2019). Magnetic mineralogical approach for the exploration of gas hydrates in the Bay of Bengal. *J. Geophys. Res. Solid Earth.* 124, 4428–4451. doi:10.1029/2019JB01746

Bastia, R. (2007). *Geologic settings and petroleum systems of India's east coast offshore basins: concepts and applications.* Bangalore, India: Tech. Pub.

Bayon, G., Dupré, S., Ponzevera, E., Etoubleau, J., Chéron, S., Pierre, C., et al. (2013). Formation of carbonate chimneys in the Mediterranean Sea linked to deep-water oxygen depletion. *Nat. Geosci.* 6 (9), 755–760. doi:10.1038/ngeo1888

Bayon, G., Henderson, G. M., Etoubleau, J., Caprais, J. C., Ruffine, L., Marsset, T., et al. (2015). U-Th isotope constraints on gas hydrate and pockmark dynamics at the Niger delta margin. *Mar. Geol.* 370, 87–98. doi:10.1016/j.margeo.2015.10.012

Berndt, C., Feseker, T., Treude, T., Krastel, S., Liebetrau, V., Niemann, H., et al. (2014). Temporal constraints on hydrate-controlled methane seepage off Svalbard. *Science.* 343 (6168), 284–287. doi:10.1126/science.1246298

Berner, R. A. (1967). Thermodynamic stability of sedimentary iron sulfides. *Am. J. Sci.* 265 (9), 773–785. doi:10.2475/ajs.265.9.773

Bian, Y., Feng, D., Roberts, H. H., and Chen, D. (2013). Tracing the evolution of seep fluids from authigenic carbonates: Green Canyon, northern Gulf of Mexico. *Mar. Petrol. Geol.* 44, 71–81. doi:10.1016/j.marpetgeo.2013.03.010

Biksham, G., and Subramanian, V. (1988). Sediment transport of the Godavari River basin and its controlling factors. *J. Hydrol.* 101 (1–4), 275–290. doi:10.1016/0022-1694(88)90040-6

Bloemendal, J., King, J. W., Hall, F. R., and Doh, S. J. (1992). Rock magnetism of late Neogene and Pleistocene deep-sea sediments: relationship to sediment source, diagenetic processes, and sediment lithology. *J Geophys. Res. Solid Earth.* 96, 4361–4375. doi:10.1029/91JB03068

Boetius, A., Ravenschlag, K., Schubert, C. J., Rickert, D., Widdel, F., Gieseke, A., et al. (2000). A marine microbial consortium apparently mediating anaerobic oxidation of methane. *Nature.* 407 (6804), 623–626. doi:10.1038/35036572

Bohrmann, G., Greinert, J., Suess, E., and Torres, M. (1998). Authigenic carbonates from the Cascadia subduction zone and their relation to gas hydrate stability. *Geology.* 26 (7), 647–650. doi:10.1130/0091-7613(1998)026<0647:ACFTCS>2.3.CO;2

Borowski, W. S., Paull, C. K., and Ussler, W., III (1996). Marine pore-water sulfate profiles indicate *in situ* methane flux from underlying gas hydrate. *Geology.* 24 (7), 655–658. doi:10.1130/0091-7613(1996)024<0655:MPWSPI>2.3.CO;2.

Chang, L., Heslop, D., Roberts, A. P., Rey, D., and Mohamed, K. J. (2016). Discrimination of biogenic and detrital magnetite through a double Verwey transition temperature. *J. Geophys. Res. Solid Earth.* 121, 3–14. doi:10.1002/2015JB012485

Chang, L., Roberts, A. P., Rowan, C. J., Tang, Y., Pruner, P., Chen, Q., et al. (2009). Low-temperature magnetic properties of greigite (Fe3S4). *Geochem. Geophys. Geosys.* 10, Q01Y04. doi:10.1029/2008GC002276

Choudhuri, M., Guha, D., Dutta, A., Sinha, S., and Sinha, N. (2010). "Spatio-temporal variations and kinematics of shale mobility in the Krishna-Godavari basin, India," in AAPG Hedberg Conference, Port of Spain,Trinidad and Tobago, June 5–7, 2006.

Chuvilin, E., Bukhanov, B., Davletshina, D., Grebenkin, S., and Istomin, V. (2018). Dissociation and self-preservation of gas hydrates in permafrost. *Geosciences.* 8 (12), 431. doi:10.3390/geosciences8120431

Clennell, M. B., Hovland, M., Booth, P. H., and Winters, W. J. (1999). Formation of natural gas hydrates in marine sediments: 1. Conceptual model of gas hydrate growth conditioned by host sediment properties. *J. Geophys. Res. Solid Earth.* 104 (B10), 22985–22003. doi:10.1029/1999JB900175

Collett, T., Riedel, M., Cochran, J. R., Boswell, R., Presley, J., Kumar, P., et al. (2008). Indian national gas hydrate Program, expedition - 01, initial report. India: Directorate General of Hydrocarbons, Ministry of Petroleum and Natural Gas.

Crémière, A., Chand, S., Sahy, D., Thorsnes, T., Martma, T., Noble, S. R., et al. (2018). Structural controls on seepage of thermogenic and microbial methane since the last glacial maximum in the Harstad Basin, southwest Barents Sea. *Mar. Petrol. Geol.* 98, 569–581. doi:10.1016/j.marpetgeo.2018.07.010

Crémière, A., Lepland, A., Chand, S., Sahy, D., Condon, D. J., Noble, S. R., et al. (2016). Timescales of methane seepage on the Norwegian margin following collapse of the Scandinavian Ice Sheet. *Nat. Commun.* 7 (1), 1–10. doi:10.1038/ncomms11509

Dela Pierre, F., Martire, L., Natalicchio, M., Clari, P., and Petrea, C. (2010). Authigenic carbonates in Upper Miocene sediments of the Tertiary Piedmont Basin (NW Italy): vestiges of an ancient gas hydrate stability zone? *Geol. Soc. Am. Bull.* 122 (7–8), 994–1010. doi:10.1130/B30026.1

Dewangan, P., Basavaiah, N., Badesab, F. K., Usapkar, A., Mazumdar, A., Joshi, R., et al. (2013). Diagenesis of magnetic minerals in a gas hydrate/cold seep environment off the Krishna–Godavari basin, Bay of Bengal. *Mar. Geol.* 340, 57–70. doi:10.1016/j.margeo.2013.04.016

Dewangan, P., Ramprasad, T., Ramana, M. V., Mazumdar, A., Desa, M., and Badesab, F. K. (2010). Seabed morphology and gas venting features in the continental slope region of Krishna-Godavari basin, Bay of Bengal: implications in gas-hydrate exploration. *Mar. Petrol. Geol.* 27 (7), 1628–1641. doi:10.1016/j.marpetgeo.2010.03.015

Dewangan, P., Sriram, G., Kumar, A., Mazumdar, A., Peketi, A., Mahale, V. P., et al. (2020). Widespread occurrence of methane seeps in deep-water regions of Krishna-Godavari basin, Bay of Bengal. *Mar. Petrol. Geol., In Press, Journal Pre-proof.* doi:10.1016/j.marpetgeo.2020.104783

Dewangan, P., Sriram, G., Ramprasad, T., Ramana, M. V., and Jaiswal, P. (2011). Fault system and thermal regime in the vicinity of site NGHP-01-10, Krishna–Godavari basin, Bay of Bengal. *Mar. Petrol. Geol.* 28, 1899–1914. doi:10.1016/j.marpetgeo.2011.03.009

Dickens, G. R. (2001). Sulfate profiles and barium fronts in sediment on the Blake Ridge: present and past methane fluxes through a large gas hydrate reservoir. *Geochem. Cosmochim. Acta.* 65 (4), 529–543. doi:10.1016/S0016-7037(00)00556-1

Dillon, M., and Bleil, U. (2006). Rock magnetic signatures in diagenetically altered sediments from the Niger deep-sea fan. *J. Geophys. Res. Solid Earth.* 111 (B3), B03105. doi:10.1029/2004JB003540

Egeberg, P. K., and Dickens, G. R. (1999). Thermodynamic and pore water halogen constraints on gas hydrate distribution at ODP Site 997 (Blake Ridge). *Chem. Geol.* 153 (1), 53–79. doi:10.1016/S0009-2541(98)00152-1

Feng, D., and Chen, D. (2015). Authigenic carbonates from an active cold seep of the northern South China Sea: new insights into fluid sources and past seepage activity. *Deep Sea Res. II.* 122, 74–83. doi:10.1016/j.dsr2.2015.02.003

Garming, J. F. L., Bleil, U., and Riedinger, N. (2005). Alteration of magnetic mineralogy at the sulfate–methane transition: analysis of sediments from the Argentine continental slope. *Phys. Earth Planet. In.* 151 (3–4), 290–308. doi:10.1016/j.pepi.2005.04.001

Geersen, J., Scholz, F., Linke, P., Schmidt, M., Lange, D., Behrmann, J. H., et al. (2016). Fault zone controlled seafloor methane seepage in the rupture area of the 2010 M aule earthquake, Central Chile. *Geochem. Geophys. Geosys.* 17 (11), 4802–4813. doi:10.1002/2016GC006498

Ginsburg, G., Soloviev, V., Matveeva, T., and Andreeva, I. (2000). "24. Sediment grain-size control on gas hydrate presence, sites 994, 995 and 997," in Paper presented at the Proceedings of the Ocean Drilling Program, Scientific Results, College Station, TX.

Greinert, J., Bohrmann, G., and Suess, E. (2001). Gas hydrate-associated carbonates and methane-venting at Hydrate Ridge: classification, distribution and origin of authigenic lithologies. *AGU.* 124, 99–114. doi:10.1029/GM124p0099

Gullapalli, S., Dewangan, P., Kumar, A., Dakara, G., and Mishra, C. K. (2019). Seismic evidence of free gas migration through the gas hydrate stability zone (GHSZ) and active methane seep in Krishna-Godavari offshore basin. *Mar. Petrol. Geol.* 110, 695–705. doi:10.1016/j.marpetgeo.2019.07.052

Han, X., Suess, E., Liebetrau, V., Eisenhauer, A., and Huang, Y. (2014). Past methane release events and environmental conditions at the upper continental slope of the South China Sea: constraints by seep carbonates. *Int. J. Earth Sci.* 103 (7), 1873–1887. doi:10.1007/s00531-014-1018-5

Handwerger, A. L., Rempel, A. W., and Skarbek, R. M. (2017). Submarine landslides triggered by destabilization of high-saturation hydrate anomalies. *Geochem. Geophys. Geosys.* 18 (7), 2429–2445. doi:10.1002/2016GC006706

Haq, B. U. (1998). Natural gas hydrates: searching for the long-term climatic and slope-stability records. *Geol. Soc. Spec. Publ.* 137 (1), 303–318. doi:10.1144/GSL.SP.1998.137.01.24

Harrison, R. J., and Feinberg, J. M. (2008). FORCinel: an improved algorithm for calculating first order reversal curve distributions using locally weighted regression smoothing. *Geochem. Geophys. Geosys.* 9, Q05016. doi:10.1029/2008GC001987

Henriet, J. P., De Mol, B., Pillen, S. T., Vanneste, M., Van Rooij, D., Versteeg, W., et al. (1998). Gas hydrate crystals may help build reefs. *Nature.* 391 (6668), 648–649. doi:10.1038/35530

Hirt, A. M., Lowrie, W., Clendenen, W. S., and Kligfield, R. (1993). Correlation of strain and the anisotropy of magnetic susceptibility in the Onaping Formation: evidence for a near-circular origin of the Sudbury basin. *Tectonophysics.* 225 (4), 231–254. doi:10.1016/0040-1951(93)90300-9

Horng, C. S. (2018). Unusual magnetic properties of sedimentary pyrrhotite in methane-seepage sediments: comparison with metamorphic pyrrhotite and sedimentary greigite. *J. Geophys. Res. Solid Earth.* 123, 4601–4617. doi:10.1002/2017JB015262

Housen, B. A., and Moskowitz, B. M. (2006). Depth distribution of magnetofossils in near-surface sediments from the Blake/Bahama Outer Ridge, western North Atlantic Ocean, determined by low-temperature magnetism. *J. Geophys. Res Biogeo.* 111, G01005. doi:10.1029/2005JG000068

Housen, B. A., and Musgrave, R. J. (1996). Rock-magnetic signature of gas hydrates in accretionary prism sediments. *Earth Planet. Sci. Lett.* 139 (3–4), 509–519. doi:10.1016/0012-821X(95)00245-8

Hu, Y., Luo, M., Liang, Q., Chen, L., Feng, D., Yang, S., et al. (2019). Pore fluid compositions and inferred fluid flow patterns at the Haima cold seeps of the South China Sea. *Mar. Petrol. Geol.* 103, 29–40. doi:10.1016/j.marpetgeo.2019.01.007

Jørgensen, B. B., Böttcher, M. E., Lüschen, H., Neretin, L. N., and Volkov, I. I. (2004). Anaerobic methane oxidation and a deep H_2S sink generate isotopically heavy sulfides in Black Sea sediments. *Geochim. Cosmochim. Acta.* 68 (9), 2095–2118. doi:10.1016/j.gca.2003.07.017

Kao, S. J., Horng, C. S., Roberts, A. P., and Liu, K. K. (2004). Carbon–sulfur–iron relationships in sedimentary rocks from southwestern Taiwan: influence of geochemical environment on greigite and pyrrhotite formation. *Chem. Geol.* 203 (1–2), 153–168. doi:10.1016/j.chemgeo.2003.09.007

Karlin, R., and Levi, S. (1983). Diagenesis of magnetic minerals in recent haemipelagic sediments. *Nature.* 303 (5915), 327. doi:10.1038/303327a0

Kars, M., and Kodama, K. (2015). Rock magnetic characterization of ferrimagnetic iron sulfides in gas hydrate-bearing marine sediments at Site C0008, Nankai Trough, Pacific Ocean, off-coast Japan. *Earth Planets Space.* 67 (1), 118. doi:10.1186/s40623-015-0287-y

Kasten, S., Freudenthal, T., Gingele, F. X., and Schulz, H. D. (1998). Simultaneous formation of iron-rich layers at different redox boundaries in sediments of the Amazon deep-sea fan. *Geochim. Cosmochim. Acta.* 62, 2253–2264. doi:10.1016/S0016-7037(98)00093-3

Kasten, S., Zabel, M., Heuer, V., and Hensen, C. (2003). "Processes and signals of nonsteady-state diagenesis in deep-sea sediments and their pore waters," in *The South Atlantic in the late quaternary.* (Berlin, Heidelberg: Springer), 431–459. doi:10.1016/j.gca.2007.08.019

Kocherla, M., Teichert, B. M. A., Pillai, S., Satyanarayanan, M., Ramamurty, P. B., Patil, D. J., et al. (2015). Formation of methane-related authigenic carbonates in a highly dynamic biogeochemical system in the Krishna–Godavari Basin, Bay of Bengal. *Mar. Petrol. Geol.* 64, 324–333. doi:10.1016/j.marpetgeo.2015.02.034

Larrasoaña, J. C., Roberts, A. P., Musgrave, R. J., Gràcia, E., Piñero, E., Vega, M., et al. (2007). Diagenetic formation of greigite and pyrrhotite in gas hydrate marine sedimentary systems. *Earth Planet Sci. Lett.* 261 (3–4), 350–366. doi:10.1016/j.epsl.2007.06.032

Lascu, I., Einsle, J. F., Ball, M. R., and Harrison, R. J. (2018). The vortex state in geologicmaterials: a micromagnetic perspective. *J. Geophys. Res. Solid Earth.* 123, 7285–7304. doi:10.1029/2018JB015909

Levin, L. A., Baco, A. R., Bowden, D. A., Colaco, A., Cordes, E. E., Cunha, M. R., et al. (2016). Hydrothermal vents and methane seeps: rethinking the sphere of influence. *Front. Mar. Sci.* 3, 72. doi:10.3389/fmars.2016.00072

Liang, Q., Hu, Y., Feng, D., Peckmann, J., Chen, L., Yang, S., et al. (2017). Authigenic carbonates from newly discovered active cold seeps on the northwestern slope of the South China Sea: constraints on fluid sources, formation environments, and seepage dynamics. *Deep-Sea Res. I.* 124, 31–41. doi:10.1016/j.dsr.2017.04.015

Liu, J., Zhu, R., Roberts, A. P., Li, S., and Chang, J. H. (2004). High-resolution analysis of early diagenetic effects on magnetic minerals in post-middle-Holocene continental shelf sediments from the Korea Strait. *J. Geophys. Res. Solid Earth.* 109 (B3), B03130 (1-15). doi:10.1029/2003JB002813

Lorenson, T. (2000). "Microscopic character of marine sediment containing disseminated gas hydrate: examples from the Blake Ridge and the Middle America Trench," in *Gas hydrates: challenges for the future.* Editors G. D. Holder and P. R. Bishnoi (New York, NY: Academy of Sciences), Vol. 912, 189–194.

Maher, B. A. (1988). Magnetic properties of some synthetic sub-micron magnetites. *Geophys. J. Int.*, 94 (1), 83-96. doi:10.1111/j.1365-246X.1988.tb03429.x

Maher, B. A., and Thompson, R. (1999). *Quaternary climates, environments and magnetism.* Cambridge, UK: Cambridge University Press.

Mazumdar, A., Dewangan, P., Joäo, H. M., Peketi, A., Khosla, V. R., Kocherla, M., et al. (2009). Evidence of paleo–cold seep activity from the Bay of Bengal, offshore India. *Geochem. Geophys. Geosys.* 10, 10Q06005. doi:10.1029/2008GC002337

Mazumdar, A., Dewangan, P., Peketi, A., Gullapalli, S., Kalpana, M. S., Naik, G. P., et al. (2019). The first record of active methane (cold) seep ecosystem associated with shallow methane hydrate from the Indian EEZ. *J. Earth. Syst. Sci.* 128, 18. doi:10.1007/s12040-018-1044-y

Mazumdar, A., Dewangan, P., Peketi, A., Gullapalli, S., Sai PavanVolvoikar, S., et al. (2018). "Methane cold seep activity in the Indian EEZ: present is the key to the past."in Indian Geophysical Union, 55th Annual Convention on Changing Water Cycle and Water Resources, December 5–7, 2018, Bhopal: Rabindranath Tagore University.

Mazzini, A., Svensen, H., Hovland, M., and Planke, S. (2006). Comparison and implications from strikingly different authigenic carbonates in a Nyegga complex pockmark, G11, Norwegian Sea. *Mar. Geol.* 231 (1–4), 89–102. doi:10.1016/j.margeo.2006.05.012

Moskowitz, B. M., Frankel, R. B., and Bazylinski, D. A. (1993). Rock magnetic criteria for the detection of biogenic magnetite. *Earth Planet Sci. Lett.* 120 (3–4), 283–300. doi:10.1016/0012-821X(93)90245-5

Musgrave, R. J., Bangs, N. L., Larrasoaña, J. C., Gràcia, E., Hollamby, J. A., and Vega, M. E. (2006). Rise of the base of the gas hydrate zone since the last glacial recorded by rock magnetism. *Geology.* 34 (2), 117–120. doi:10.1130/G22038.1

Musgrave, R. J., Kars, M., and Vega, M. E. (2019). Progressive and punctuated magnetic mineral diagenesis: the rock magnetic record of multiple fluid inputs and progressive pyritization in a volcano-bounded basin, IODP site U1437, Izu rear arc. *J. Geophys. Res. Solid Earth.* 124 (6), 5357–5378. doi:10.1029/2018JB017277

Muxworthy, A. R., and Dunlop, D. J. (2002). First-order reversal curve (FORC) diagrams for pseudo-single-domain magnetites at high temperature. *Earth Planet Sci. Lett.* 203 (1), 369–382. doi:10.1016/S0012-821X(02)00880-4

Muxworthy, A. R., and McClelland, E. (2000). Review of the low-temperature magnetic properties of magnetite from a rock magnetic perspective. *Geophys. J. Int.* 140 (1), 101–114. doi:10.1046/j.1365-246x.2000.00999.x

Naehr, T. H., Rodriguez, N. M., Bohrmann, G., Paull, C. K., and Botz, R. (2000). "29. Methanederived authigenic carbonates associated with gas hydrate decomposition and fluid venting above the Blake Ridge Diapir," in Proceedings of the Ocean Drilling Program, Scientific Results, Vol. 164, 285–300.

Neretin, L. N., Böttcher, M. E., Jørgensen, B. B., Volkov, I. I., Lüschen, H., and Hilgenfeldt, K. (2004). Pyritization processes and greigite formation in the advancing sulfidization front in the upper Pleistocene sediments of the Black Sea 1. *Geochim. Cosmochim. Acta.* 68 (9), 2081–2093. doi:10.1016/S0016-7037(03)00450-2

Nowaczyk, N. R., Arz, H. W., Frank, U., Kind, J., and Plessen, B. (2012). Dynamics of the laschamp geomagnetic excursion from black sea sediments. *Earth Planet. Sc. Lett.* 351–352, 54–69. doi:10.1016/j.epsl.2012.06.050

Özdemir, Ö., and Dunlop, D. J. (1997). Effect of crystal defects and internal stress on the domain structure and magnetic properties of magnetite. *J. Geophys. Res. Solid Earth.* 102 (B9), 20211–20224. doi:10.1029/97JB01779

Özdemir, Ö., Dunlop, D. J., and Moskowitz, B. M. (2002). Changes in remanence, coercivity and domain state at low temperature in magnetite. *Earth Planet Sci. Lett.* 194 (3–4), 343–358. doi:10.1016/S0012-821X(01)00562-3

Passier, H. D., De Lange, G. J., and Dekkers, M. J. (2001). Magnetic properties and geochemistry of the active oxidation front and the youngest sapropel in the eastern Mediterranean Sea. *Geophys. J. Int.* 145 (3), 604–614. doi:10.1046/j.0956-540x.2001.01394.x

Passier, H. F., Dekkers, M. J., and de Lange, G. J. (1998). Sediment chemistry and magnetic properties in an anomalously reducing core from the eastern Mediterranean Sea. *Chem. Geol.* 152 (3–4), 287–306. doi:10.1016/S0009-2541(98)00121-1

Passier, H. F., and Dekkers, M. J. (2002). Iron oxide formation in the active oxidation front above sapropel S1 in the eastern Mediterranean Sea as derived from low-temperature magnetism. *Geophys. J. Int.* 150 (1), 230–240. doi:10.1046/j.1365-246X.2002.01704.x

Peketi, A., Mazumdar, A., Joshi, R. K., Patil, D. J., Srinivas, P. L., and Dayal, A. M. (2012). Tracing the paleo sulfate–methane transition zones and H_2S seepage events in marine sediments: an application of C-S-Mo systematic. *Geochem. Geophys. Geosys.* 13, Q10007. doi:10.1029/2012GC004288

Peters, C., and Dekkers, M. J. (2003). Selected room temperature magnetic parameters as a function of mineralogy, concentration and grain size. *Phys Chem Earth A/B/C.* 28 (16–19), 659–667. doi:10.1016/S1474-7065(03)00120-7

Peters, C., and Thompson, R. (1998). Magnetic identification of selected natural iron oxides and sulphides. *J. Magn. Magn. Mater.* 183 (3), 365–374. doi:10.1016/S0304-8853(97)01097-4

Petersen, N., Von Dobeneck, T., and Vali, H. (1986). Fossil bacterial magnetite in deep-sea sediments from the South Atlantic Ocean. *Nature.* 320, 611–615. doi:10.1038/320611a0

Philips, S. C. (2018). Diagenetic degradation of paleoenvironmental signals in magnetic susceptibility in the northern Bay of Bengal. *IRM Quart.* 27 (4).

Pierre, C., and Fouquet, Y. (2007). Authigenic carbonates from methane seeps of the Congo deep-sea fan. *Geo Mar. Lett.* 27 (2–4), 249–257. doi:10.1007/s00367-007-0081-3

Pike, C. R., Roberts, A. P., and Verosub, K. L. (1999). Characterizing interactions in fine magnetic particle systems using first order reversal curves. *J. Appl. Phys.* 85 (9), 6660–6667. doi:10.1063/1.370176

Powell, C. M., Roots, S. R., and Veevers, J. J. (1988). Pre-breakup continental extension in East Gondwanaland and the early opening of the eastern Indian Ocean. *Tectonophysics.* 155, 261–283. doi:10.1016/0040-1951(88)90269-7

Prabhakar, K. N., and Zutshi, P. L. (1993). Evolution of southern part of Indian East Coast basin. *J. Geol. Soc. India.* 41, 215–230.

Ramesh, R., and Subramanian, V. (1988). Temporal, spatial and size variation in the sediment transport in the Krishna River basin, India. *J Hydrol.* 98, 53–65. doi:10.1016/0022-1694(88)90205-3

Rao, G. N., and Mani, K. S. (1993). A study on generation of abnormal formation pressures in Krishna-Godavari Basin, India. *Indian J. Pet. geol.* 2, 20–30.

Rao, G. N. (2001). Sedimentation, stratigraphy, and petroleum potential of Krishna-Godavari basin, east coast of India. *Am. Assoc. Pet. Geol. Bull.* 85 (9), 1623–1643. doi:10.1306/8626CCDF-173B-11D7-8645000102C1865D

Rao, V. P. (1991). Clay mineral distribution in the continental shelf sediments from Krishna to Ganges river mouth, east coast of India. *Indian J. Mar. Sci.* 20, 7–12.

Rees, E. V. L., Priest, J. A., and Clayton, C. R. I. (2011). The structure of methane gas hydrate bearing sediments from the Krishna-Godavari Basin as seen from micro-CT scanning. *Mar. Petrol. Geol.* 28 (7), 1283–1293. doi:10.1016/j.marpetgeo.2011.03.015

Riedinger, N., Pfeifer, K., Kasten, S., Garming, J. F. L., Vogt, C., and Hensen, C. (2005). Diagenetic alteration of magnetic signals by anaerobic oxidation of methane related to a change in sedimentation rate. *Geochim. Cosmochim. Acta.* 69 (16), 4117–4126. doi:10.1016/j.gca.2005.02.004

Roberts, A. P., Almeida, T. P., Church, N. S., Harrison, R. J., Heslop, D., Li, Y., et al. (2017). Resolving the origin of pseudo-single domain magnetic behavior. *J. Geophys. Res. Solid Earth.* 122, 9534–9558. doi:10.1002/2017JB014860

Roberts, A. P., Chang, L., Rowan, C. J., Horng, C. S., and Florindo, F. (2011). Magnetic properties of sedimentary greigite (Fe_3S_4): an update. *Rev. Geophys.* 49, RG1002. doi:10.1029/2010RG000336

Roberts, A. P. (2015). Magnetic mineral diagenesis. *Earth Sci. Rev.* 151, 1–47. doi:10.1016/j.earscirev.2015.09.010

Roberts, A. P. (1995). Magnetic properties of sedimentary greigite (Fe_3S_4). *Earth Planet. Sci. Lett.* 134 (3), 227–236. doi:10.1016/0012-821X(95)00131-U

Roberts, A. P., Pike, C. R., and Verosub, K. L. (2000). First-order reversal curve diagrams: a new tool for characterizing the magnetic properties of natural samples. *J. Geophys. Res. Solid Earth.* 105 (B12), 28461–28475. doi:10.1029/2000JB900326

Roberts, A. P., Stoner, J. S., and Richter, C. (1999). Diagenetic magnetic enhancement of sapropels from the eastern Mediterranean Sea. *Mar. Geol.* 153 (1-4), 103-116. doi:10.1016/S0025-3227(98)00087-5

Roberts, A. P., Zhao, X., Harrison, R. J., Heslop, D., Muxworthy, A. R., Rowan, C. J., et al. (2018). Signatures of reductive magnetic mineral diagenesis from unmixing of first-order reversal curves. *J. Geophys. Res. Solid Earth.* 123, 4500–4522. doi:10.1029/2018JB015706

Rowan, C. J., Roberts, A. P., and Broadbent, T. (2009). Reductive diagenesis, magnetite dissolution, greigite growth and paleomagnetic smoothing in marine sediments: a new view. *Earth Planet Sci. Lett.* 277 (1–2), 223–235. doi:10.1016/j.epsl.2008.10.016

Rowan, C. J., and Roberts, A. P. (2006). Magnetite dissolution, diachronous greigite formation, and secondary magnetizations from pyrite oxidation: unravelling complex magnetizations in Neogene marine sediments from New Zealand. *Earth Planet Sci. Lett.* 241 (1–2), 119–137. doi:10.1016/j.epsl.2005.10.017

Sahling, H., Römer, M., Pape, T., Bergès, B., dos Santos Fereirra, C., Boelmann, J., et al. (2014). Gas emissions at the continental margin west of Svalbard: mapping, sampling, and quantification. *Biogeosciences.* 11 (21), 6029–6046. doi:10.5194/bg-11-6029-2014

Sangode, S. J., Sinha, R., Phartiyal, B., Chauhan, O. S., Mazari, R. K., Bagati, T. N., et al. (2007). Environmental magnetic studies on some quaternary sediments of varied depositional settings in the Indian sub-continent. *Quat. Int.* 159, 102–118. doi:10.1016/j.quaint.2006.08.015

Schneider, A., Panieri, G., Lepland, A., Consolaro, C., Crémière, A., Forwick, M., et al. (2018). Methane seepage at Vestnesa Ridge (NW Svalbard) since the last glacial maximum. *Quat. Sci. Rev.* 193, 98–117. doi:10.1016/j.quascirev.2018.06.006

Sellanes, J., and Krylova, E. (2005). A new species of *Calyptogena* (Bivalvia: Vesicomyidae) from a recently discovered methane seepage area off Concepción Bay, Chile (~ 36 S). *J. Mar. Biolog. Assoc. U.K.* 85 (4), 969–976. doi:10.1017/S0025315405011963

Singha, D. K., and Chatterjee, R. (2014). Detection of overpressure zones and a statistical model for pore pressure estimation from well logs in the Krishna-Godavari Basin, India. *Geochem. Geophys. Geosys.* 15 (4), 1009–1020. doi:10.1002/2013GC005162

Snowball, I., and Thompson, R. (1990). A stable chemical remanence in Holocene sediments. *J. Geophys. Res. Solid Earth.* 95, 4471–4479. doi:10.1029/JB095iB04p04471

Snyder, G. T., Hiruta, A., Matsumoto, R., Dickens, G. R., Tomaru, H., Takeuchi, R., et al. (2007). Pore water profiles and authigenic mineralization in shallow marine sediments above the methane-charged system on Umitaka Spur, Japan Sea. *Deep-Sea Res. II.* 54 (11–13), 1216–1239. doi:10.1016/j.dsr2.2007.04.001

Sriram, G., Dewangan, P., Kumar, A., Mazumdar, A., Peketi, A., and Mahale, V. P. (2020). "Structural control on the methane seeps and shallow gas hydrate deposits in Krishna – Godavari Basin, Bay of Bengal," in 36th International Geological Congress, November 9–14, 2020.

Sriram, G., Dewangan, P., Ramprasad, T., and Rama Rao, P. (2013). Anisotropic amplitude variation of the bottom-simulating reflector beneath fracture-filled gas hydrate deposit. *J. Geophys. Res. Solid Earth.* 118 (5), 2258–2274. doi:10.1002/jgrb.50176

Suess, E. (2014). Marine cold seeps and their manifestations: geological control, biogeochemical criteria and environmental conditions. *Int. J. Earth Sci.* 103 (7), 1889–1916. doi:10.1007/s00531-014-1010-0

Sultan, N., Cochonat, P., Foucher, J. P., and Mienert, J. (2004). Effect of gas hydrates melting on seafloor slope instability. *Mar. Geol.* 213 (1), 379–401. doi:10.1016/j.margeo.2004.10.015

Tarduno, J. A., Sager, W. W., and Nogi, Y. (1995). "Early cretaceous magnetostratigraphy and paleolatitudes from the mid-pacific mountains: preliminary results bearing on guyot formation and pacific plate translation," in *Proc. ODP, Sci. Results.* Editors E. L. Winterer, W. W. Sager, J. V. Firth, and J. M. Sinton (College Station, TX: Ocean Drilling Program), Vol. 143, 395–398.

Tarduno, J. A. (1995). Superparamagnetism and reduction diagenesis in pelagic sediments: enhancement or depletion? *Geophys. Res. Lett.* 22 (11), 1337–1340. doi:10.1029/95GL00888

Teichert, B. M. A., and Luppold, F. W. (2013). Glendonites from an Early Jurassic methane seep-Climate or methane indicators? *Palaeogeogr. Palaeoclimatol. Palaeoecol.* 390, 81–93. doi:10.1016/j.palaeo.2013.03.001

Tong, H., Feng, D., Cheng, H., Yang, S., Wang, H., Min, A. G., et al. (2013). Authigenic carbonates from seeps on the northern continental slope of the South China Sea: new insights into fluid sources and geochronology. *Mar. Petrol. Geol.* 43, 260–271. doi:10.1016/j.marpetgeo.2013.01.011

Torres, M. E., McManus, J., Hammond, D. E., De Angelis, M. A., Heeschen, K. U., Colbert, S. L., et al. (2002). Fluid and chemical fluxes in and out of sediments hosting methane hydrate deposits on Hydrate Ridge, OR, I: hydrological provinces. *Earth Planet Sci. Lett.* 201 (3–4), 525–540. doi:10.1016/S0012-821X(02)00733-1

Torres, M. E., Trehu, A. M., Cespedes, N., Kastner, M., Wortmann, U. G., Kim, J. H., et al. (2008). Methane hydrate formation in turbidite sediments of northern Cascadia, IODP Expedition 311. *Earth Planet Sci. Lett.* 271, 170–180. doi:10.1016/j.epsl.2008.03.061

Usapkar, A., Dewangan, P., Kocherla, M., Ramprasad, T., Mazumdar, A., and Ramana, M. V. (2014). Enhanced methane flux event and sediment dispersal pattern in the Krishna–Godavari offshore basin: evidences from rock magnetic techniques. *Mar. Petrol. Geol.* 58, 461–475. doi:10.1016/j.marpetgeo.2014.08.008

Vadakkepuliyambatta, S., Bünz, S., Mienert, J., and Chand, S. (2013). Distribution of subsurface fluid-flow systems in the SW Barents Sea. *Mar. Petrol. Geol.* 43, 208–221. doi:10.1016/j.marpetgeo.2013.02.007

Verwey, E. J. W. (1939). Electronic conduction of magnetite (Fe_3O_4) and its transition point at low temperatures. *Nature.* 144 (3642), 327. doi:10.1038/144327b0

Vogt, P. R., and Jung, W. Y. (2002). Holocene mass wasting on upper non-Polar continental slopes—due to post-Glacial ocean warming and hydrate dissociation? *Geophy. Res. Lett.* 29 (9), 55–61. doi:10.1029/2001GL013488

Weinberger, J. L., and Brown, K. M. (2006). Fracture networks and hydrate distribution at Hydrate Ridge, Oregon. *Earth Planet Sci. Lett.* 245, 123–136. doi:10.1016/j.epsl.2006.03.012

Wellsbury, P., Goodman, K., Cragg, B. A., and Parkes, R. J. (2000). "The geomicrobiology of deep marine sediments from Blake Ridge containing methane hydrate (Sites 994, 995 and 997)," in Proceedings of the Ocean drilling program, Scientific results, College Station, TX: ODP, Vol. 164, 379–391. doi:10.1029/2001GL013488

Wilkin, R. T., and Barnes, H. L. (1997). Formation processes of framboidal pyrite. *Geochim. Cosmochim. Acta.* 61 (2), 323–339. doi:10.1016/S0016-7037(96)00320-1

Yao, H., Hong, W. L., Panieri, G., Sauer, S., Torres, M. E., Lehmann, M. F., et al. (2019). Fracture-controlled fluid transport supports microbial methane-oxidizing communities at Vestnesa Ridge. *Biogeosciences.* 16, 2221–2232. doi:10.5194/bg-16-2221-2019

You, K., Flemings, P. B., Malinverno, A., Collett, T. S., and Darnell, K. (2019). Mechanisms of methane hydrate formation in geological systems. *Rev. Geophys.* 57 (4), 1146–1196. doi:10.1029/2018RG000638